THE UNIVERSITY OF WARWICK

AUTHOR: **Earl Davis** DEGREE: **M.Sc.**

TITLE: **Chemical Treatment to Reduce Electron Accumulation at InN Surfaces**

DATE OF DEPOSIT: ....

I agree that this thesis shall be available in accordance with the regulations governing the University of Warwick theses.

I agree that the summary of this thesis may be submitted for publication.

I **agree** that the thesis may be photocopied (single copies for study purposes only).

Theses with no restriction on photocopying will also be made available to the British Library for microfilming. The British Library may supply copies to individuals or libraries. subject to a statement from them that the copy is supplied for non-publishing purposes. All copies supplied by the British Library will carry the following statement:

> "Attention is drawn to the fact that the copyright of this thesis rests with its author. This copy of the thesis has been supplied on the condition that anyone who consults it is understood to recognise that its copyright rests with its author and that no quotation from the thesis and no information derived from it may be published without the author's written consent."

AUTHOR'S SIGNATURE: ....

USER'S DECLARATION

1. I undertake not to quote or make use of any information from this thesis without making acknowledgement to the author.

2. I further undertake to allow no-one else to use this thesis while it is in my care.

DATE SIGNATURE ADDRESS

....

....

....

....

....

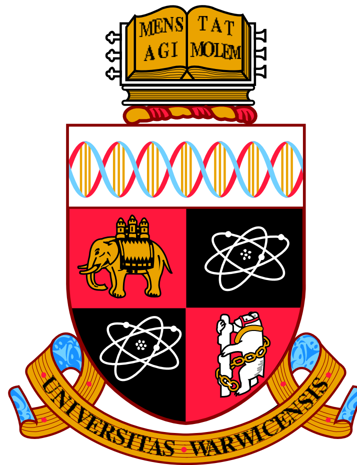

Chemical Treatment to Reduce Electron Accumulation at InN Surfaces

by

Earl Davis

Thesis

Submitted to the University of Warwick

for the degree of

Master of Science

Department of Physics

September 2013

THE UNIVERSITY OF
WARWICK

Contents

List of Figures **iii**

Acknowledgments **v**

Declarations **vii**

Abstract **ix**

Abbreviations **x**

Chapter 1 Introduction **1**

1.1 Indium nitride and related alloys 1
1.2 Crystal structure of InN 3
1.3 History of the InN bandgap 5
1.4 Surface electron accumulation 7
1.4.1 Charge neutrality level 8
1.4.2 Space charge region 11
1.5 Surface structure of InN 14
1.6 Surface treatment 15
1.7 Thesis organisation 16

Chapter 2 Experimental Methods **18**

2.1 X-ray photoelectron spectroscopy 18
2.1.1 Features of an XPS spectrum 20
2.1.2 Chemical shifts 24
2.1.3 Quantification from XPS 24
2.1.4 Calibration 26

2.1.5 Spectrometer 27
2.2 Hall effect measurements 27
2.2.1 Van der Pauw Geometry 29

Chapter 3 Theoretical Methods 32
3.1 Band structure approximations 32
3.1.1 Parabolic approximation 32
3.1.2 k.p perturbation theory 33
3.2 Poisson's equation 35
3.2.1 Modified Thomas-Fermi approximation (MTFA) 36

Chapter 4 Ex-situ Sulfur Treatment of InN Surfaces 40
4.1 Introduction 40
4.2 Experimental Details 41
4.3 Results and Analysis 41
4.4 Conclusions 46

Chapter 5 In-situ Sulfur Deposition on InN Surfaces 47
5.1 Introduction 47
5.2 Experimental details 48
5.3 Results and analysis 52
5.3.1 *a*-plane InN 52
5.3.2 In-polar *c*-plane InN 59
5.3.3 Comparison of *a*-plane and In-polar *c*-plane InN 67
5.4 Conclusions 68

Chapter 6 Summary and Conclusions 69
6.1 Future Directions 71

Bibliography 71

List of Figures

1.1 The band gaps of InGaN alloys. 2
1.2 The wurtzite crystal structure of InN. 3
1.3 The crystallographic faces of InN. 4
1.4 Brillouin zone for hexagonal crystals. 4
1.5 Optical absorption measurements on InN. 5
1.6 Optical measurements showing lower band gap of InN. 6
1.7 Illustration demonstrating the Burstein-Moss shift. 7
1.8 Charge carrier density profile for Mg-doped p-type InN. 8
1.9 InN band structure across the Brillouin zone 11
1.10 Band bending at InN surface. 12
1.11 ARPES showing quantization of electron accumulation layer. . 13
1.12 Indium adlayers and reconstruction at the In-polar *c*-plane surface. 14

2.1 Universal curve for attenuation length. 19
2.2 XPS schematic 19
2.3 Example XPS binding energy spectrum for InN. 21
2.4 Example fitting of K 2p doublet peak. 22
2.5 Example valence band XPS spectrum. 23
2.6 XPS energy level diagram. 26
2.7 Hall effect 28
2.8 Van der Pauw geometry. 30

3.1 Numerically calculated band bending profile. 37
3.2 Numerically calculated charge carrier concentration profile. . . 38

4.1 Valence band region for S_2Cl_2 treated InN samples 42

4.2 Charge carrier profile for S_2Cl_2 treated InN samples 42
4.3 S 2p region of disulfur dichloride treated samples. 43
4.4 N 1s region the untreated and S_2Cl_2 treated InN samples . . . 44
4.5 O 1s region the untreated and S_2Cl_2 treated InN samples . . . 46

5.1 Survey spectrum after preparation. 49
5.2 XPS spectra of InN post HCl etch and annealing. 50
5.3 LEED image from cleaned InN. 51
5.4 Electrochemical sulfur cell schematic. 51
5.5 Valence band spectra and VBM-E_F separation throughout sulfur deposition – *a*-plane sample. 53
5.6 Band bending and charge carrier concentration profiles. 54
5.7 Decrease in conduction band plasmon losses. 55
5.8 S 2p region after first and final sulfur deposition. 57
5.9 Development of the S 2p region as sulfur is deposited. 58
5.10 Valence band spectra and VBM-E_F separation throughout sulfur deposition – *c*-plane sample. 60
5.11 Band bending and charge carrier concentration profile with sulfur. 62
5.12 Decrease in conduction band plasmon losses. 63
5.13 S 2p regions of XPS spectrum after sulfur depositions. 64
5.14 Development of the S 2p region as sulfur is deposited. 65

Acknowledgments

First thanks should go to my supervisor Chris McConville for the giving me the opportunity to become acquainted with vacuum science and study the wonderful, quirky material that is indium nitride. Thanks also go to my surprise second supervisor, Mark-with-a-'c' Walker, for help with XPS measurements, some close shaves with the CAICISS chamber transfers, car rides to the pub, cake, and the tea club (I will settle my bill, honest!).

I must also thank the other past and present members of P459 for many great (and sometimes traumatic) memories. James 'Labview' Mudd for introducing me to IGOR and to all things photoemission, the perennially angry Christopher Burrows for unprecedented levels of sarcasm and rudeness (and for kindly helping me out with accommodation at the end of my course) and Nessa Fereshteh-Saniee, my thesis-writing buddy, for many entertaining procrastinatory conversations. Of course, my time at Warwick would not have been the same without the entertainment provided by our summer students. Thanks to Sophie Rennie, who lives in Advantage West Midlands, for ensuring my mug was clean, Mike Mills for outrageous banter amd scarring my mind with his maid outfit, blink-and-you'll-miss-him-Jack Hills and Ben "Want it? Can't have it" Slater. The dishonorary group member, Mohammed Saghir, is greatly thanked for laughter he brought to the office and for being my canary-down-the-master's-degree-mine.

Thanks also go to the other members of the group who I have had the

pleasure of spending time with. Gavin “Pub?” Bell, Sepehr Farahani – the boxing enthusiast, Sean “Paul” McMitchell, Daesung Park, Haiyuan Wang, Ouserigha Collins, Aleksander Krupski and Katarzyna Miskow. Of course, this list would not be complete without mention of the legendary Robert Johnston, group technician and worker of miracles.

A huge thanks must go to my extended family at Elim Pentecostal Church, Coventry. I had an amazing five years of serving, learning and growing as part of the church. I also met wonderful people who have walked alongside me through the good and bad times. The staff at the Village Hotel who made my time working there bearable are also thanked.

I wouldn’t be where I am without my amazing family who have supported me every step in every way. I love you so much and thank you from the bottom of my heart.

Lastly, but most importantly, I thank God for the grace He has shown towards me and for His faithfulness in all things. This is all for You.

Declarations

I declare that this thesis contains an account of my research carried out in the Department of Physics at the University of Warwick between October 2011 and September 2013 under the supervision of Prof. C. F. McConville. The research reported here has not been submitted either wholly or in part in this or any other academic institution for the admission to a higher degree.

The XPS measurements presented in chapter 5 were in part made by Dr Marc Walker and Mr James Mudd. The program used to perform the band bending and charge carrier concentration profiles is a modified version of the code written by Dr Tim Veal and Dr Wojciech Linhart, adapted for use in the IgorPRO software by Mr James Mudd. The remaining data collection, data fitting, data analysis and calculations was performed solely by the author.

Earl Davis

November 2013

The work presented in this thesis has also been presented at the following international conference.

E. M. Davis, M. Walker, J. J. Mudd, L. R. Bailey, C. F. McConville, H. Lu, W. J. Schaff,
Sulfur Passivation of InN Surfaces (oral presentation)
29th European Conference on Surface Science (ECOSS-29)
September 2012, Edinburgh, UK.

Abstract

The modification and control of the electronic properties of semiconducting InN surfaces has been investigated by x-ray photoelectron spectroscopy (XPS) and Hall effect measurements. The fundamental properties of InN and its ternary alloys InGaN and InAlN make it a promising material for use in opto-electronic and electronic devices that operate in the THz frequency band. However, the intrinsic electron accumulation observed at the surfaces and interfaces of InN and any high In-content alloys presents significant difficulties when trying to incorporate this material into devices. This is due to the charge neutrality level (CNL) of the semiconductor lying high above the conduction band minimum (CBM) at the centre of the Brillouin zone. Ex-situ sulfur treatment using ammonium polysulfide ($(NH_4)S_x$) solution, commonly used for several other III-V compounds, has been found to reduce the downward band bending of undoped InN by as much as 0.15 eV and decrease the surface sheet charge density by 30 %. In-situ passivation, however, is preferable as the surface can be studied without exposure to contaminants.

In this work, ex-situ treatment of InN with disulfur dichloride (S_2Cl_2) solution and in-situ sulfur deposition on the surfaces of InN using a silver sulfide electrochemical cell has been studied. The one-electron potential and carrier concentration profile have been calculated for an accumulation layer at the surface of the semiconductor. This is achieved by solving Poisson's equation within a modified Thomas-Fermi approximation and numerically solving the Schrödinger equation for the resulting potential well. Kane's $\mathbf{k}\cdot\mathbf{p}$ approximation for a non-parabolic conduction band is also incorporated in the model.

The results of these experiments showed that a reduction in electron accumulation of 53 % was achieved for S_2Cl_2 treatment of an In-polar *c*-plane InN sample, however, control of the treatment proved to be difficult. For the in-situ treatment, deposition of sulfur resulted in a complete removal of the electron accumulation layer for the *a*-plane sample and a 55 % reduction in the electron accumulation was achieved for the In-polar *c*-plane sample. It is also shown that an In–S–S–In bonding environment creates a greater reduction in electron accumulation than In–S–In bonding.

Abbreviations

ADM amphoteric defect model

CBM conduction band minimum

CNL charge neutrality level

CAICISS co-axial impact collision ion scattering spectroscopy

DFT density functional theory

DOS density of states

FWHM full-width at half-maximum

IMFP inelastic mean free path

LEED low energy electron diffraction

MTFA modified Thomas-Fermi approximation

PAMBE plasma assisted molecular beam epitaxy

QPC-DFT quasi-particle corrected density functional theory

STM scanning tunnelling microscopy

UHV ultra-high vacuum

VBM valence band maximum

ViGS virtual gap states

XPS x-ray photoelectron spectroscopy

ξ separation of the valence band maximum and Fermi level at the surface

Chapter 1

Introduction

1.1 Indium nitride and related alloys

For many years, technological advancements have been intimately tied to improved understanding and application of semiconductor materials. Although silicon remains the semiconductor most commonly used in electronic devices, III-V semiconductors such as GaAs and InSb have also come to prominence for optoelectronic applications and high-frequency electronic devices [1, 2]. This is due to their (generally) direct band gaps, low electron effective masses and high electron mobilities. However, development has created the need for new materials that can achieve higher speeds and, with innovative design, push the boundaries of photonic and high-frequency devices even further.

Indium nitride and its related alloys, InGaN and InAlN, present an excellent example of III-V semiconductors with high predicted electron mobilities [3, 4] and velocities [5] for electronic and optoelectronic device applications. InN itself has many potential applications, such as terahertz emitters and near infrared optoelectronic device applications [6–9]. Additionally, due to the band gap of InN (~0.65 eV) lying in the infrared and the bandgaps of GaN (~3.44 eV) and AlN (~6.25 eV) lying in the ultra-violet and extreme ultra-violet respectively, the ternary alloys InGaN and InAlN have composition-dependent bandgaps that span the entire visible spectrum [10–12], shown in Figure 1.1. Multijunction solar cells using two or more InGaN compositions could theoretically have quantum efficiencies of up to 70 % [14–17]. Moreover, these alloys are less toxic than the currently used GaInP/GaInAs systems, and

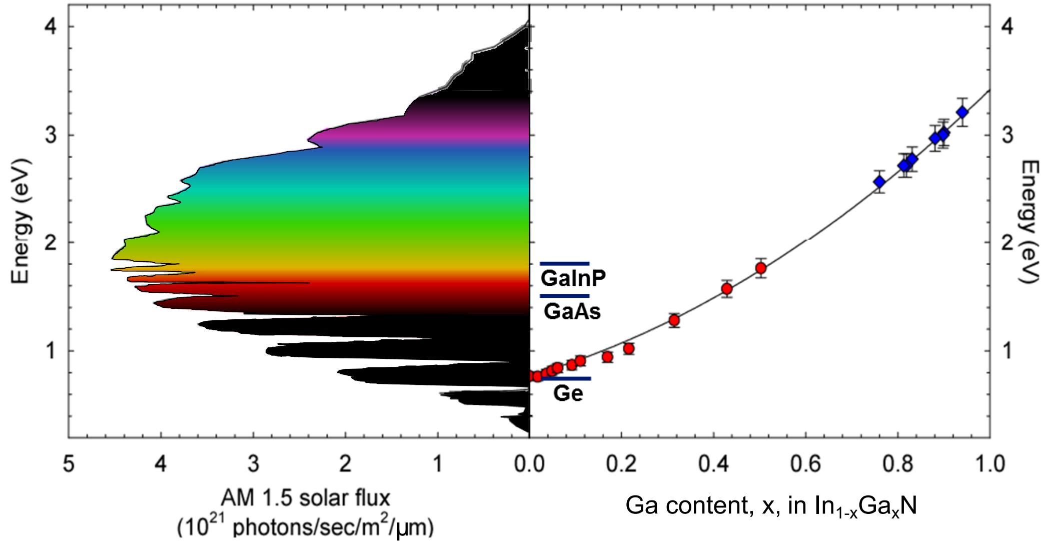

Figure 1.1: Compositionally dependent matching of InGaN alloys to the visible spectrum, showing great promise for multijunction solar cell devices [13]. For comparison, the band gaps of one of the current best multijunction devices, a GaInP–GaAs–Ge system, is shown. It can be seen that InGaN alloys have much potential to improve device efficiency through a much greater range of the visible spectrum.

are also relatively unaffected by large lattice mismatches and defect concentrations. This leads to InGaN alloys being much more resistant to radiation, and thus offer great potential for applications in space and other harsh environments, where efficiency and durability replace cost as the most important characteristic for devices [13]. GaN and Ga-rich InGaN are already widely used commercially in ultra-violet light-emitting diodes (LEDs) and laser diodes in Blu-ray DVD players, and in 2009, researchers at Nichia Corporation produced the first stable InGaN green laser diode [18, 19].

Despite all of the advantages, the development of devices using InN and high In-content alloys has been restricted due to several problematic properties. As grown InN exhibits a high propensity for n-type doping, making p-type doping a significant challenge. Moreover, both n- and p-type InN have a large intrinsic electron accumulation layer at the surface. This means that InN makes almost exclusively Ohmic contacts, making the manufacture of Schottky devices requiring tunnel junctions difficult [20–22]. The electron accumulation also leads to the bulk of p-type InN being electrically isolated from

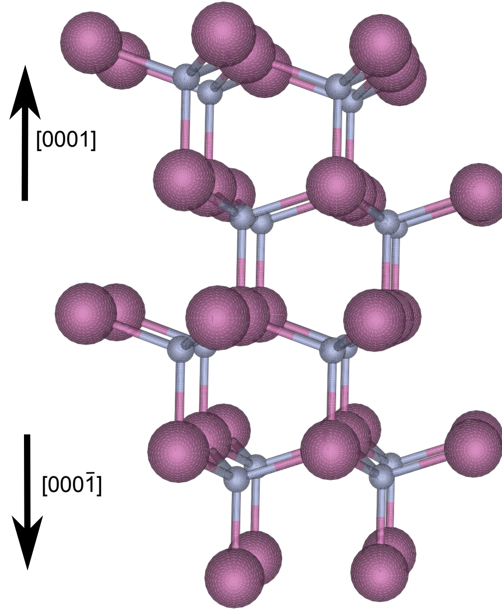

Figure 1.2: The wurtzite crystal structure of indium (purple) nitride (blue). Made using VESTA software for crystal visualisation [24].

the surface, preventing contact with the bulk [23].

1.2 Crystal structure of InN

InN crystallises in two different polymorphs, wurtzite (hexagonal) and zinc-blende (cubic), however, in this thesis only wurtzite InN has been investigated. In the wurtzite structure, each In atom is tetrahedrally bonded to four N atoms (and vice versa), as shown in Figure 1.2, forming planes of In and N atoms perpendicular to the c-axis.

Throughout this thesis four-index Miller-Bravais notation is used to describe the surface directions due to the non-orthogonality of the crystallographic directions a and b in the hexagonal wurtzite crystal structure. In this notation $(h\,k\,i\,l)$ denotes a plane that intercepts the axes at $\frac{a}{h}$, $\frac{b}{k}$, $\frac{c}{l}$, and the dummy index $i = -(h + k)$. The dummy index helps to reveal symmetries within the structure, for example, the $(1\,1\,\bar{2}\,0)$ plane is equivalent to the $(1\,\bar{2}\,1\,0)$ and $(\bar{2}\,1\,1\,0)$ planes. From this basis, $[h\,k\,i\,l]$ denotes the real-space direction perpendicular to the $(h\,k\,i\,l)$ plane.

The $[0\,0\,0\,1]$ and $[0\,0\,0\,\bar{1}]$ directions in a wurtzite crystal are distinguish-

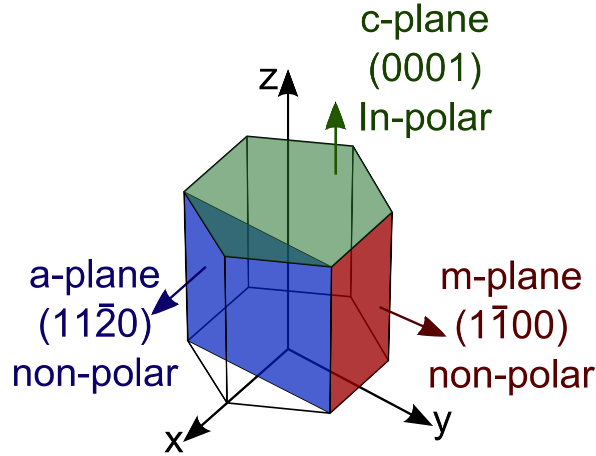

Figure 1.3: Diagram illustrating the crystallographic faces of InN and their respective notations.

able, with In-polarity (N-polarity) defined such that the crystal is orientated with only a single bond from the In (N) atom directed toward the surface along the c-axis. Both InN(0 0 0 1) and InN(0 0 0 $\bar{1}$) naturally terminate with a layer of In atoms [25]. Henceforth the (0 0 0 1) plane are denoted as In-polar c-plane, the (0 0 0 $\bar{1}$) plane as N-polar c-plane, and the (1 1 $\bar{2}$ 0) and (1 $\bar{1}$ 0 0) planes will be denoted as a-plane and m-plane respectively. These planes are illustrated in Figure 1.3.

It is worth briefly mentioning the crystal structure in reciprocal space. The first Brillouin zone is used for Bloch descriptions of waves in the periodic crystal structure, and is shown for a hexagonal crystal along with the naming conventions for points in Figure 1.4.

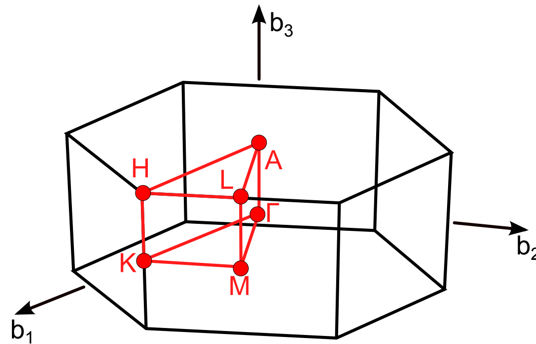

Figure 1.4: The first Brillouin zone and its key points for the hexagonal crystal structure, where b_i are the reciprocal lattice vectors.

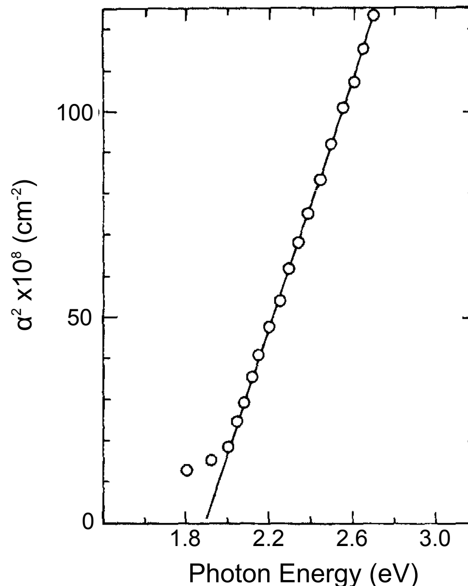

Figure 1.5: Optical absorption measurements made by Tansley and Foley to determine the band gap of InN [30]. The square of the absorption coefficient, α, was plotted against photon energy and extrapolated to give a band gap energy value of 1.9 eV. These measurements were made using a low quality polycrystalline sample with an electron concentration of 1.6×10^{16} cm^{-3}.

1.3 History of the InN bandgap

Until the early 2000s, it was believed that the bandgap of InN was close to 1.9 eV. The samples were grown before this time using radio-frequency sputtering [26], and this method of growth created polycrystalline samples with high electron concentrations [27] and significant oxygen contamination [28]. They also exhibited low electron mobilities in the 10-100 cm^2/Vs range. The widely used band gap value of 1.9 eV [29] came as a result of optical absorption measurements showing a strong absorption band in the infrared and an absorption edge at about 1.9 eV [30] (shown in Figure 1.5). However, the lack of light emission from near the band edge remained unexplained.

More recently, improvement in growth methods for InGaN and InAlN films using metal-organic vapor phase epitaxy (MOVPE) resulted in a dramatic increase in the quality of these nitride films [31]. It was unexpectedly found that the band gaps of InGaN and InAlN alloys rapidly decreased to well below 2 eV with increasing In content when extrapolated for higher indium

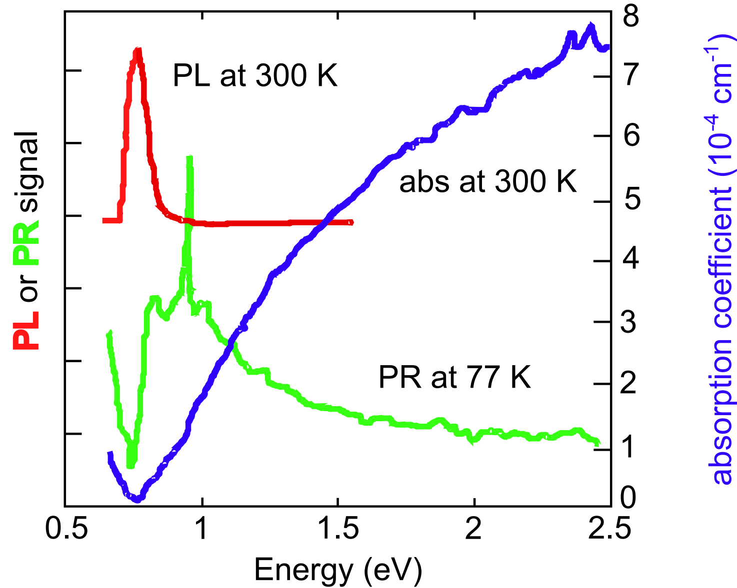

Figure 1.6: Optical absorption measurements made by Wu et al. providing evidence of a lower band gap for InN and photoluminescence (PL) and photoreflectance (PR) supporting this new value. [11].

concentrations [32, 33], however, this was generally attributed to an unusually large bowing parameter, such as the coupling of photons with plasmon modes [32].

The breakthrough came with the arrival of InN samples grown by plasma assisted molecular beam epitaxy (PAMBE) [34–36]. This allowed high-quality thick films to be grown with reduced electron concentrations and higher electron mobilities. Measurements of the band gap of InN was firstly reduced to 0.9 eV [35], then to 0.77 eV (see Figure 1.6) [11], before converging at 0.65 eV [37], with photoluminesence and photoreflectance also being observed at this value.

It emerged that the reason for the previous high band gap of InN was due to oxygen doping and a Burstein-Moss shift [38, 39], accentuated by the unexpectedly low electron effective mass, and low density of states (DOS) near the conduction band minimum (CBM). This effect is shown in Figure 1.7, where, due to the high defect densities and high electron concentrations in the polycrystalline samples, the states up to the Fermi level high in the conduction band were filled, meaning that electrons in the valence band could not be

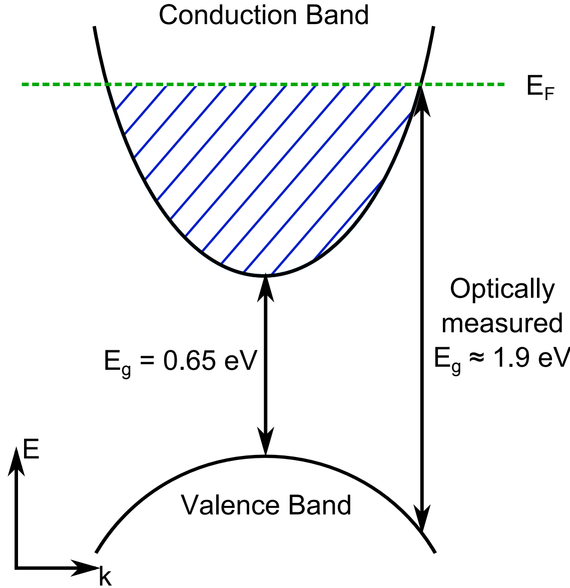

Figure 1.7: Illustration demonstrating the Burstein-Moss shift, the cause of the incorrect assignment of the band gap, E_g, of InN at 1.9 eV, where E_F is the Fermi level.

excited to those occupied states across the direct bandgap at the Γ-point. Therefore, the observed absorption edge was a measurement of electrons being excited from the valence band elsewhere in the Brillouin zone.

1.4 Surface electron accumulation

Both p- and n-type indium nitride have been universally observed to exhibit an intrinsic electron accumulation layer at the surface due to large downward bending of the valence band maximum (VBM) and CBM. This enables Ohmic contact to be made easily to n-type InN, however, the existence of an inversion layer prevents contact with the bulk in p-type InN as can be seen in the charge carrier density profile in Figure 1.8. Here, the lack of charge carriers between 95-110 nm prevents charge flow between the bulk and the surface. This electron accumulation layer also prevents the formation of Schottky contacts, essential for many potential device applications. The presence of an electron accumulation layer at the surface of InN is closely related to the presence of virtual gap states (ViGS), the position of an energy level called the charge

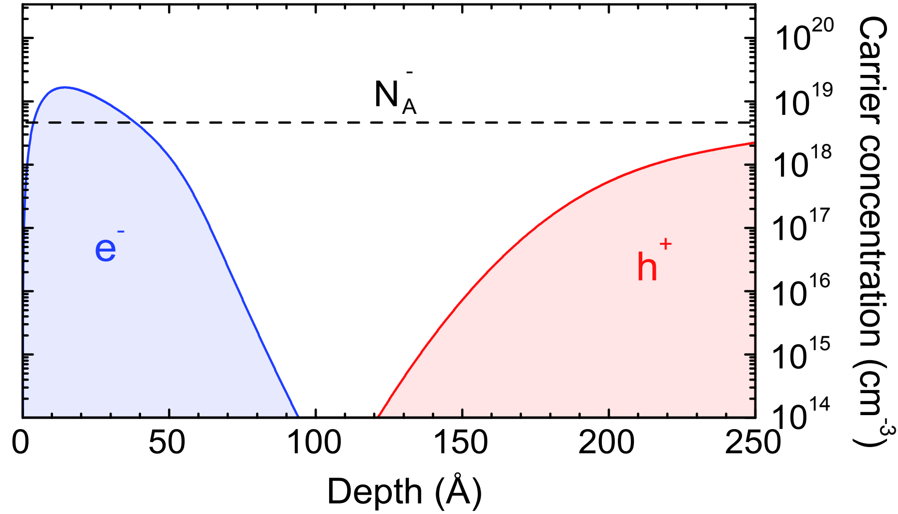

Figure 1.8: Charge carrier density profile for Mg-doped p-type InN showing electron (e^-), hole (h^+) and near-surface acceptor (N_A^-) concentrations and demonstrating the electronic isolation of the p-type bulk from the surface [23].

neutrality level (CNL) and where it lies relative to the Fermi level, and the valence and conduction band extrema.

1.4.1 Charge neutrality level

In 1989, Walukiewicz proposed the amphoteric defect model (ADM) as an explanation for the understanding of the factors affecting the quantity and reactions of native defects in semiconductors [40]. Although this model inaccurately attributes native defect states as the sole origin of the electronic properties of semiconductor surfaces, it is still useful in understanding the nature of defects arising at the surface due to the termination of the crystal potential. The nature of these defects is dependent on an where the Fermi level lies in relation to an energy level called the Fermi stabilisation energy, where defects formed while the Fermi level is below (above) the Fermi stabilisation energy are likely to be donor (acceptor)-like in nature, having real energies in the band gap but complex wavevectors. The existence of these states lying in the band gap of a semiconductor can be shown through considering solutions of the many-body Schrödinger equation describing the behaviour of electrons

in a crystal, given by

$$\hat{H}|\phi\rangle = E|\phi\rangle, \tag{1.1}$$

where $\phi(\mathbf{r}_1, \mathbf{r}_2, \mathbf{r}_3, ..., \mathbf{r}_N,)$ is an N-body wavefunction. The Hamiltonian operator, $\hat{H}$, is given by

$$\hat{H} = \sum_{i=1}^{N} \frac{\mathbf{p}_i^2}{2m_i} + \frac{1}{2} \sum_{i=1, j\neq i}^{N} \frac{Z_i Z_j}{4\pi\epsilon_0 |\mathbf{r}_i - \mathbf{r}_j|}, \tag{1.2}$$

neglecting magnetic effects, where N is the number of particles (electrons and ions) of mass m_i, charge Z_i, and spatial position $\mathbf{r}_i$, and

$$\mathbf{p}_i = -i\hbar\nabla_i \tag{1.3}$$

is the momentum operator.

Using the Born-Oppenheimer (adiabatic) approximation [41], which decouples the motion of ions from electrons, the Hamiltonian simplifies to

$$\hat{H} = \sum_{i=1} -\frac{\hbar}{2m_e}\nabla_i^2 + \frac{1}{2} \sum_{i,j=1, j\neq i} \frac{e^2}{4\pi\epsilon_0 |\mathbf{r}_i - \mathbf{r}_j|} - \sum_{i,l} \frac{Z_l e}{4\pi\epsilon_0 |\mathbf{r}_i - \mathbf{R}_{l_0}|} \tag{1.4}$$

for an N-body electronic system. The indices i, j (l) label the electrons (ions) at position $\mathbf{r}_{i,j}$ (equilibrium position $\mathbf{R}_{l_0}$), m_e is the electron mass, e is the electronic charge and Z_l is the charge of the ion core.

From this point, the one-electron approximation, where electron-electron interaction is averaged to contribute a constant repulsive component to the Hamiltonian, and the mean-field approximation, which assumes that each electron is in identical surroundings dependent on interactions with ions in their equilibrium positions [42], can be used. The band structure can then be approximated by solving Equation 1.1 with the simplified Hamiltonian

$$\hat{H} = \frac{\mathbf{p}^2}{2m_e} + V_0(\mathbf{r}), \tag{1.5}$$

where $V_0(\mathbf{r})$ is the periodic potential of the Bravais lattice. Due to the translation symmetry of the lattice, the solutions to Equation 1.5 can be shown to

be Bloch wavefunctions, plane waves of the form

$$\psi_{\nu\mathbf{k}}(\mathbf{r}) = u_{\nu\mathbf{k}}(\mathbf{r}) \exp(i\mathbf{k} \cdot \mathbf{r}), \tag{1.6}$$

where ν labels the band, $\mathbf{k}$ is the wavevector of the electron in the first Brillouin zone and the translational symmetry of the lattice is represented in the Bloch wavefunction such that

$$u_{\nu\mathbf{k}}(\mathbf{r} + \mathbf{T}) = u_{\nu\mathbf{k}}(\mathbf{r}) \tag{1.7}$$

where $\mathbf{T}$ is the translation vector.

In the bulk, the periodic boundary conditions for an infinite crystal lattice requires the Bloch wavevector to be real. However, at the surface where this periodicity is broken, states with a complex wavevector are allowed which are also solutions to the Schrödinger equation. These physically describe surface states which decay exponentially into the bulk of the semiconductor and into the vacuum. The complex dispersion of states also exists in the bulk, however, they are forbidden and are therefore termed virtual gap states (ViGS) [43]. The character of the ViGS changes from predominantly acceptor-like near the conduction band to predominantly donor-like near the valence band and the energy at which the crossover happens is termed the branch point energy of the ViGS. This occurs at the minimum decay length of the wavefunctions of the ViGS, and is found just below the mid-gap energy of the semiconductor (the average band gap integrated across the Brillouin zone) due to the ViGS being highly localised in real space, and therefore receiving a contribution in momentum space from a large proportion of the Brillouin zone. As this branching point indicates energy where states change from predominantly donor-like to predominantly acceptor-like, the branch point energy can equivalently be termed the CNL of the semiconductor [44, 45] and is believed to be universal for all materials on an absolute energy scale [46]. The CNL for InN, which has been shown experimentally to lie 1.83 ± 0.10 eV above the VBM [47], is indicated in the band-structure diagram in Figure 1.9. The band structure was calculated using quasi-particle corrected density functional theory (QPC-DFT) by Bechstedt and co-workers [47], and shows the presence of an extraordinarily low CBM at the Γ-point and the Fermi level pinning position.

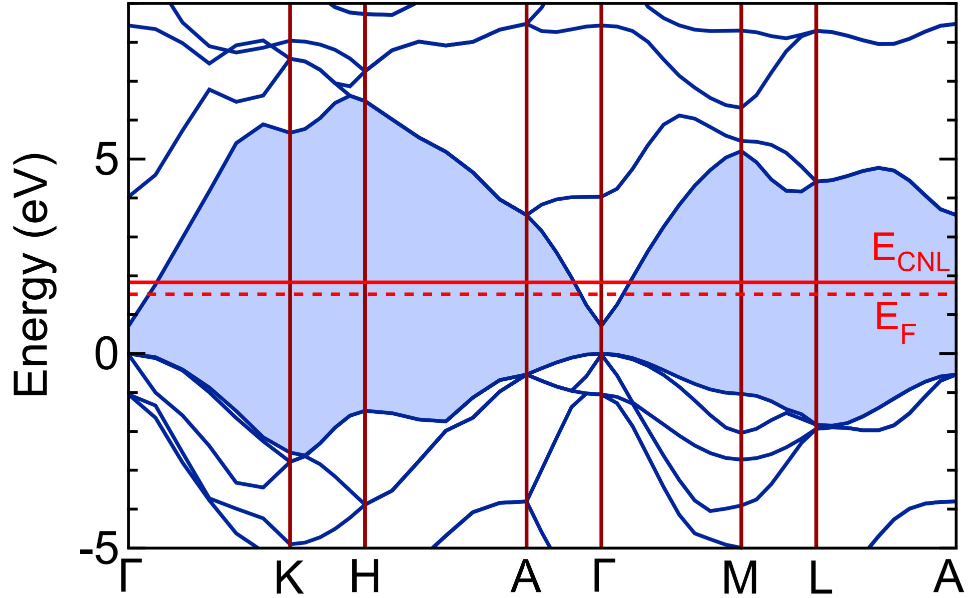

Figure 1.9: Wurtzite InN band structure across the Brillouin zone calculated using quasi-particle corrected density functional theory (QPC-DFT). The bulk Fermi level (E_F) is shown to lie above the conduction band minimum at the Γ*-point, pinned just below the CNL. [47]*

1.4.2 Space charge region

A positive point charge placed into a locally neutral electron plasma will be screened by the rearrangement of the electrons such that the electric field due to the positive charge will vanish over a given range. This range is dependent on the density of electrons, with higher densities yielding shorter screening lengths. The spatial region of redistributed electrons is called a space charge region [48]. At the surface of a crystalline solid, the symmetry of the bulk structure is terminated and the surface atoms have fewer neighbouring atoms and different chemical bonds to those in the bulk. For a semiconductor, the breakdown of the symmetry of the crystal structure may induce electronic surface states which perturb the local charge balance. The type of states (donor or acceptor) and the position of the Fermi level determine whether the surface states carry charge. Occupied donor-like states and unoccupied acceptor-like states are neutral, whereas unoccupied donor-like states are positively charged and occupied acceptor-like states are negatively charged. The position of the

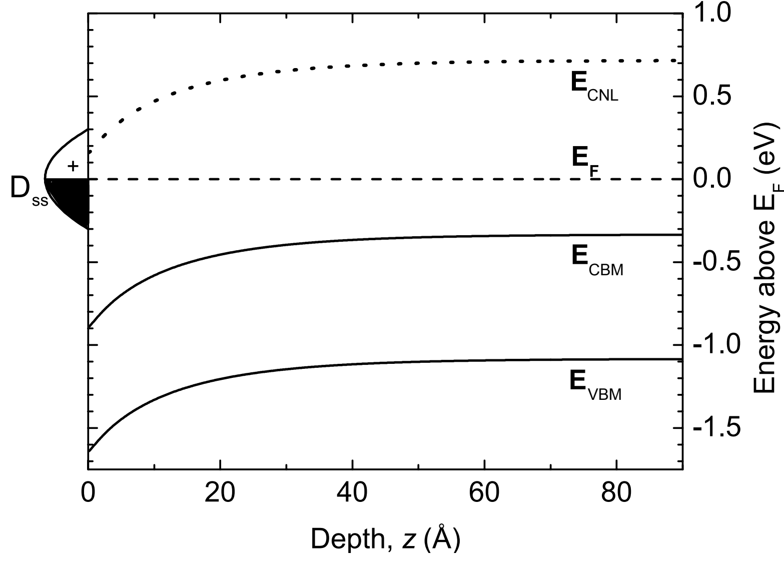

Figure 1.10: Downward band bending in InN, as the Fermi level, E_F, tends towards the CNL at the surface to maintain charge neutrality. The donor-type surface states, D_{ss}, are also shown, where the unoccupied states above the Fermi level are shown to be positively charged [49].

Fermi level at the surface is determined by the condition of charge neutrality:

$$Q_{ss} = -Q_{sc}, \tag{1.8}$$

where Q_{ss} is the charge of the surface states, which is compensated by an opposite charge, Q_{sc}, which screens the surface state charge and is called the space charge.

Figure 1.10 shows the effect of a space charge layer, i.e. downward band bending, compensating for the charge Q_{ss} of unoccupied donor-like states at the surface. Figure 1.10 can then be understood as follows: deep in the bulk of the crystal, the doping level determines the position of the Fermi level relative to the CBM. However, the high energetic positions of donor states in relation to the CBM at the surface are fixed by interatomic potentials at the surface. If there were flat bands to the surface, the Fermi level would be positioned far below the donor-like surface states. An uncompensated positive charge density would then be built up because these states would be completely empty. This situation is unstable, resulting in a space charge layer and downward band bending, which is achieved by free electrons accumulating in the conduction

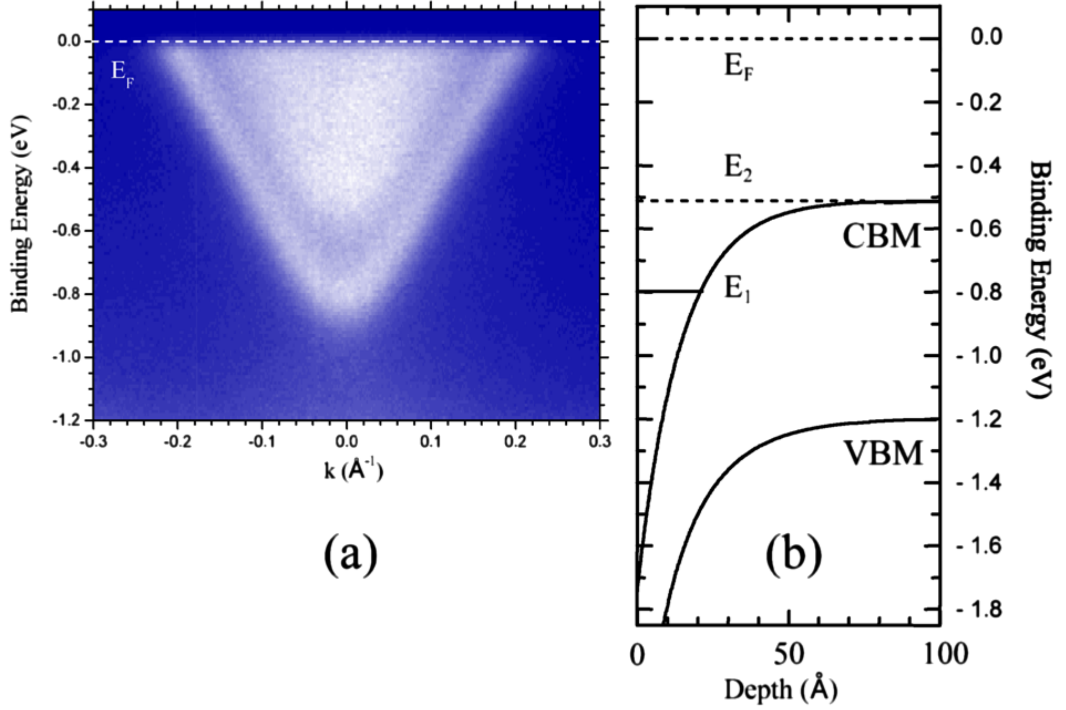

Figure 1.11: (a) Angle resolved photoemission spectroscopy (ARPES) photocurrent intensity map of states within 1.2 eV of the Fermi level (E_F) in the momentum direction ΓM in the surface plane. (b) The calculated downward band bending of the CBM and VBM with respect to E_F. E_1 and E_2, at 0.511 and 0.797 eV respectively, mark the subband minima of an exponential approximation to the surface potential well. From the work of Colakerol et al [51].

band with space charge Q_{sc} satisfying Equation 1.8.

In the case of InN, the CNL lies well above the CBM at the Γ-point (shown in Figure 1.9). This energy represents the crossover from the probability of ViGS being donor-like to being acceptor-like, and lies approximately at the average midpoint between the CBM and VBM across the Brillioun zone. The Fermi level is pinned close to this energy in the bulk. However, to maintain charge neutrality, the Fermi level tends towards the CNL at the surface, leading to downward band bending. This band bending is illustrated in Figure 1.10, and leads to the formation of an electron accumulation layer [50]. Using angle resolved photoemission spectroscopy (ARPES), the electrons in the accumulation layer have been shown to exist in discrete quantum well states, forming a two dimensional (2D) electron gas perpendicular to the surface as shown in Figure 1.11 [25].

1.5 Surface structure of InN

Independent of the surface polarity, indium adlayers have been universally observed on the growth surfaces of InN. The number of these adlayers is dependent on the crystallographic plane and polarity of the sample [52]. It has been proposed that metallic In-In bonding states in these adlayers are the microscopic origin of donor-type surface states and a source of electrons for the accumulation layer [25, 53]. This has been confirmed for *a*-plane InN samples where samples cleaved in-situ exhibited flat bands at the surface [54]. Recent work has shown that exposure of samples to adsorbants post-growth leads to an increase in band bending and electron accumulation for the N-polar *c*-plane surface [55]. This also lends weight to the idea that the formation of In adlayers is due to defects according to the ADM proposed by Walukiewicz [40, 56].

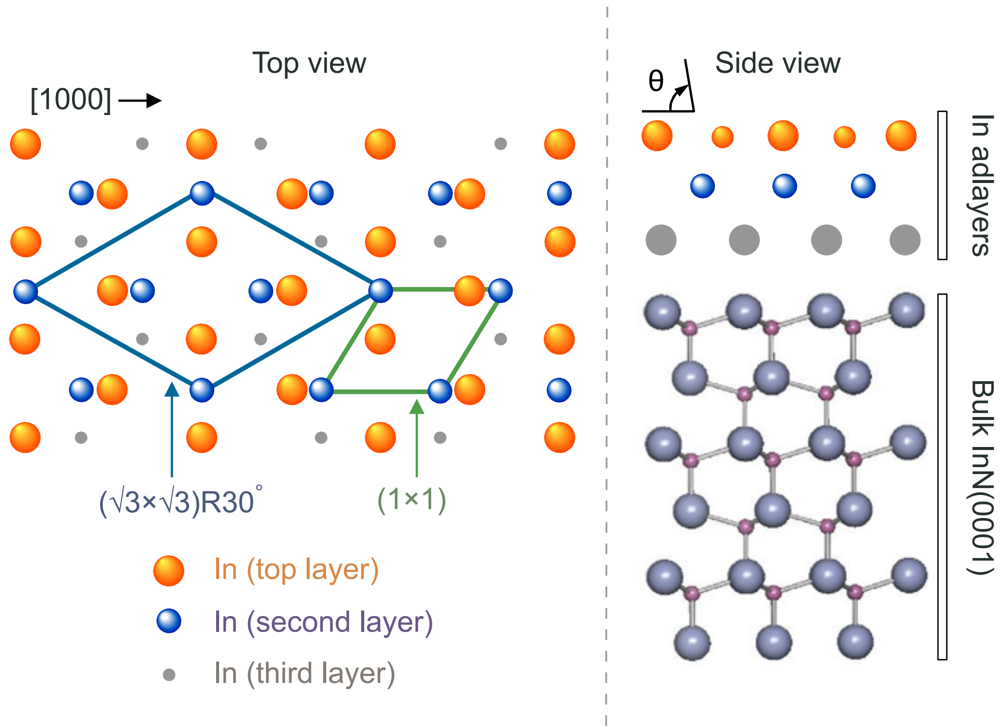

Figure 1.12: Top and side view of structural models of the indium adlayers and calculated surface reconstruction at the In-polar c-plane surface. Three layers of indium are present on top of the In-terminated bulk, with the topmost layer consisting of 4/3 monolayers of In exhibiting a $(\sqrt{3} \times \sqrt{3})R30^{\circ}$ *periodicity [57].*

Surface reconstructions have been observed on the In-polar c-plane surface, with characterisation showing the presence of ~3.4 ML (monolayers) of indium exhibiting a laterally contracted top layer with a $(\sqrt{3} \times \sqrt{3})$R30° periodicty [52, 57], drawing analogy from the Ga adlayers observed on GaN. The extent of knowledge of the structure of the adlayers at the a-plane surface is restricted to the observation of 3.0 ML of In and that in-situ removal of these adlayers eliminates band bending [52, 54].

It has been observed, however, that although the a-plane and In- and N-polar c-plane surfaces all exhibit differing In adlayer thickness, this has no effect on the separation of the valence band and the Fermi level at the surface. This is due to the metallic character of the In adlayers providing a screening for the polarisation charge caused by the bulk termination [57].

1.6 Surface treatment

Control of the electron accumulation layer at InN surfaces is crucial for the realisation of device applications and could potentially be achieved either through the deposition of a material onto the surface or through chemical treatment. For p-type InN, control may also be possible through doping effects. Any material deposited on the surface would be required to have a high electronegativity, so as to draw charge away from the InN surface, and result in a stable passivation of the surface so that its properties remain for the lifetime of any potential device. One such potential material is oxygen, and studies have shown that induced oxidation produces a marked reduction in electron concentration [58–61]. However, this thesis will focus on sulfur, which has a long history of use in surface passivation treatments of group IV, III-V and II-VI semiconductor surfaces. Sulfur has an electronegativity of 2.54 on the Pauling scale [62], which compares favourably to the value of 1.78 for indium. Amongst III-V compound semiconductors, it has been shown that sulfur bonded to the surface prevents oxidation upon exposure to air [63]. In sulfur treatment of the other III-V semiconductor exhibiting electron accumulation, InAs, sulfur occupies sites in the group V sublattice and so acts as a donor, enhancing band bending and increasing electron accumulation [64, 65]. However, sulfur has been shown to produce a reduction in band bending due to sulfur–indium

bonds formed at the surface of both n- and p-type InN [66–68]. It is able to do this because of the In adlayers stabilising the surface layer. This is the dominant force driving surface reconstruction, overriding mechanisms obeying electron counting rules and reducing the number of dangling bonds which usually govern conventional III-V semiconductor systems. These layers act to prevent the sulfur from bonding with nitrogen. On the n-type polar surfaces, this results in a ~30 % reduction of electron accumulation, whilst on p-type samples a reduction of ~70 % is observed, due to charge compensation by bulk donors. It has also been shown that this effect is stable with exposure to atmosphere for extended periods of time [69]. To date, these treatments have focussed on ex-situ chemical treatment with ammonium polysulfide ($(NH_4)_2S_x$) which does not require a clean surface and is more easily implemented in industry, but sulfur is deposited in a less controlled manner than in-situ techniques. In-situ techniques also have the advantage that time-resolved analysis of treatment is possible and the need for handling of toxic chemicals is reduced significantly.

In this thesis, x-ray photoelectron spectroscopy (XPS) and Hall effect measurements have been used to investigate previously untried sulfur treatments for InN surfaces. An ex-situ treatment using S_2Cl_2 solution has been used in an attempt to clean and passivate the surface simultaneously, whilst an in-situ deposition of sulfur has also been investigated in order to study the interaction of sulfur at the surface with significantly less contamination present and gain greater insight into the sulfur-induced modification of the electronic properties of the surface.

1.7 Thesis organisation

The remainder of this thesis will look in detail at the properties of InN, particularly at the surface and how to probe these surfaces.

Chapter 2 introduces the core experimental techniques (x-ray photoelectron spectroscopy (XPS) and Hall effect measurements) used throughout this work to investigate the bulk and surface properties of untreated and treated InN samples. The theoretical background behind these techniques is also introduced, as well as schematics for a typical experiment and example data to illustrate how analysis is carried out. The theoretical calculations that are

carried out for data analysis are outlined in chapter 3.

Chapters 4 and 5 present the results and analysis of the experimental work carried out in this thesis. Ex-situ treatment using disulfur dichloride (S_2Cl_2) solution and in-situ deposition of sulfur in chapters 4 and 5 respectively were used to reduce band bending and hence electron accumulation at the surface. The conclusions drawn from this work and potential future directions are then presented in chapter 6.

Chapter 2

Experimental Methods

Two main experimental techniques, namely XPS and single field Hall effect measurements, have been used throughout this thesis to investigate the properties of InN surfaces. This chapter describes their theoretical background and the requisite equipment.

2.1 X-ray photoelectron spectroscopy

X-ray photoelectron spectroscopy (XPS) was used to determine the surface composition and electronic properties of the InN samples before and after surface treatment. This technique takes advantage of the photoelectric effect, where a sample irradiated with a photon with an energy above a threshold interacts with an atomic orbital electron, resulting in total energy transfer and the ejection of the electron. The kinetic energy of the ejected electron is linearly related to the threshold (binding) energy of the electron within the atom, which is dependent on the element and its local bonding environment.

Although x-rays can travel through solids easily, at least 1000 nm into a sample, electrons have significantly less ability to do so due to inelastic scattering, thus limiting the escape depth of electrons and ensuring the technique is surface sensitive. The attenuation lengths for electrons with varying energy is shown in Figure 2.1. The inelastic mean free path (IMFP) of an electron can be defined as the average distance an electron of a given energy will travel between inelastic scattering events. For electrons of energies typically used in XPS, around 1 keV, the IMFP is usually between 1-4 nm. XPS is usually car-

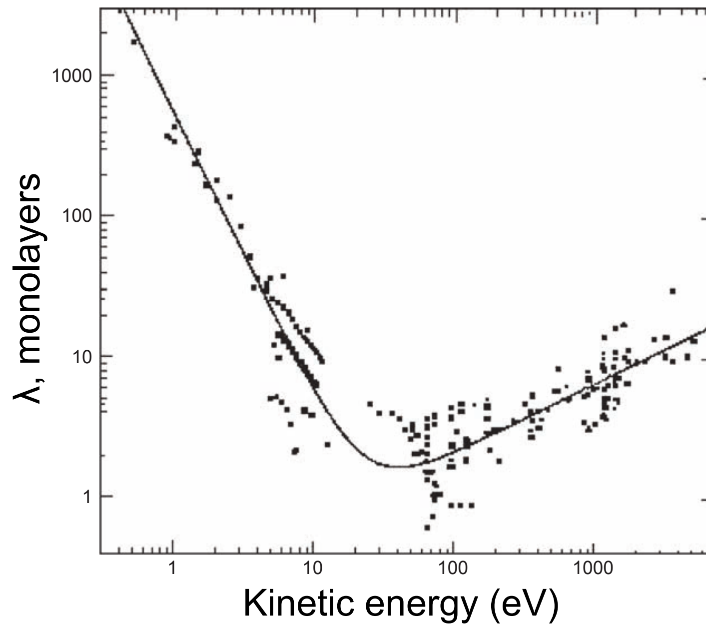

Figure 2.1: Universal curve for the dependence of attenuation length, λ, on electron kinetic energy for various elements. X-rays with energy ~1 keV are typically used in x-ray photoelectron spectroscopy (XPS). From the work of Seah and Dench [70].

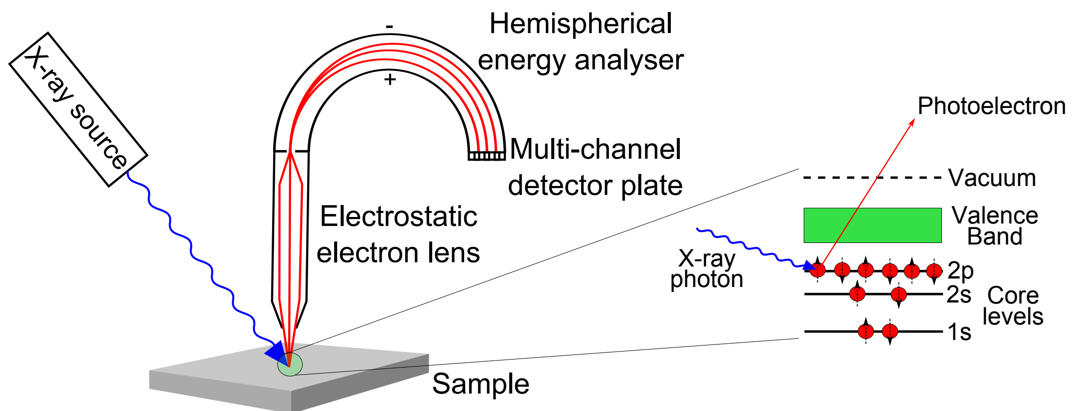

Figure 2.2: Simplified schematic showing the typical XPS experimental setup and the core level photoelectron emission process. Photons from the x-ray source are directed at the sample and interact with electrons in the core levels and valence band. These electrons receive energy from the photon and are ejected into the vacuum with this energy. The lenses focus these electrons into the analyser, which selects electrons of specific energies to be counted by the detector.

ried out under ultra-high vacuum (UHV) conditions, as the IMFP for electrons is very low at atmospheric pressures.

The kinetic energy of an ejected electron, KE, is related to the energy of the incoming photon, $h\nu$, the binding energy of the electron, E_B, and the minimum energy required to eject an electron from the Fermi level to the vacuum level, the work function of the sample, ϕ_s, by the following equation:

$$E_B = h\nu - KE - \phi_s \tag{2.1}$$

In a typical XPS experimental setup, as shown in Figure 2.2, lenses focus electrons ejected from the sample into an analyser. The kinetic energy of these electrons is measured by a hemispherical analyser with a potential applied between the inner and outer hemispheres. This potential is chosen such that the trajectory of the electrons of a specific kinetic energy is deflected into the multi-channel plate detector. This also means that electrons with a higher (lower) kinetic energy will crash into the outer (inner) plates, thereby selecting only electrons of a chosen kinetic energy. These electrons are then counted, and by sweeping the potentials on the hemisphere within the analyser, a spectrum of kinetic energy can be obtained. This spectrum can then be converted to binding energy using Equation 2.1.

2.1.1 Features of an XPS spectrum

Core level peaks

A typical XPS binding energy spectrum for an InN sample is shown in Figure 2.3, where the labelled peaks of high intensity correspond to electrons ejected from the core levels of the atoms within the sample. Every element has a unique characteristic XPS spectrum (though in practise hydrogen and helium are not easily detectable), and the area of each peak is related to the concentration of the element within the sample, giving information on chemical composition and relative quantities. The conventional notation for the labelling of these peaks is X nl_j, where X is the element, n is the principal quantum number, l is the orbital angular momentum quantum number (s = 0, p = 1, d = 2, f = 3, etc.) and j contains information about the spin of the

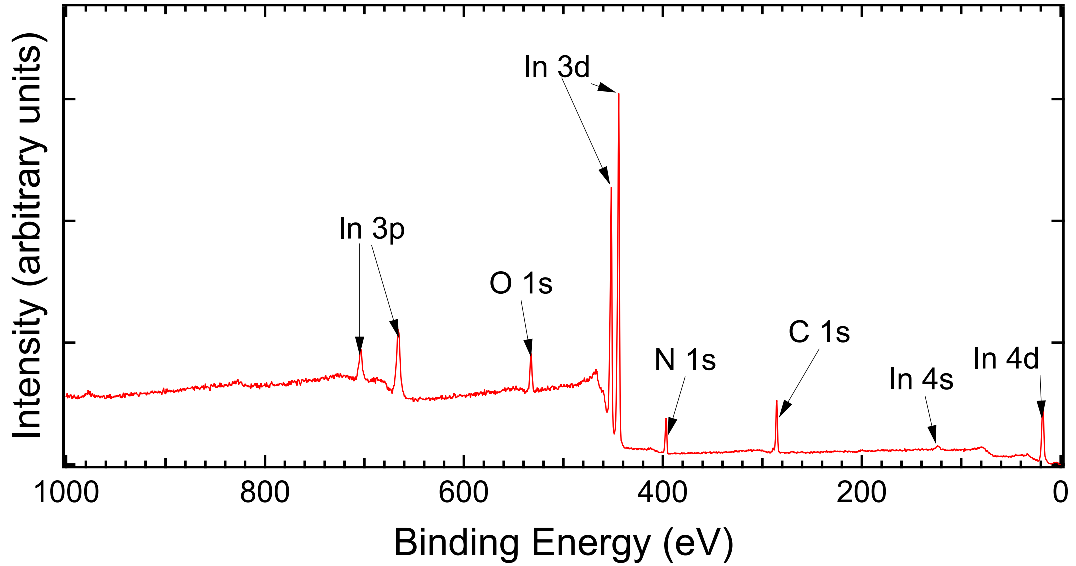

Figure 2.3: Typical binding energy spectrum of an as-loaded InN sample in XPS. The Fermi level is defined as zero on the binding energy scale. Atmospheric contamination in the form of carbon and oxygen are also seen on the surface.

electron.

For electrons where $l \neq 0$ and there are two states of the same energy (i.e. orbital degeneracy), $j = l \pm s$ where s is the spin. In this case a magnetic interaction between the orbital angular momentum and the spin of the electron can lead to a splitting of the degenerate state into two components with offset energy. This is called spin-orbit splitting, and results in a doublet peak in the XPS spectrum. The ratio of the intensity of these peaks is dependent on the ratio of their respective degeneracies, $2j + 1$.

There are several contributions to the width of a core level peak. These are principally the lifetime of the core hole, the spectral width of the photon source radiation and the analyser resolution. The peak shape can typically be described by a mixture of a Gaussian and a Lorentzian profile, called a Voigt function. Throughout this thesis, core level peaks were fitted with Voigt line-shapes using the CasaXPS data processing software [71], with a least squares fit being used for optimisation. An example of a fit for a K 2p doublet peak is given in Figure 2.4.

Another feature to be noted regarding core level peaks is the presence of plasmon losses in the spectra due to the collective vibrations of the free

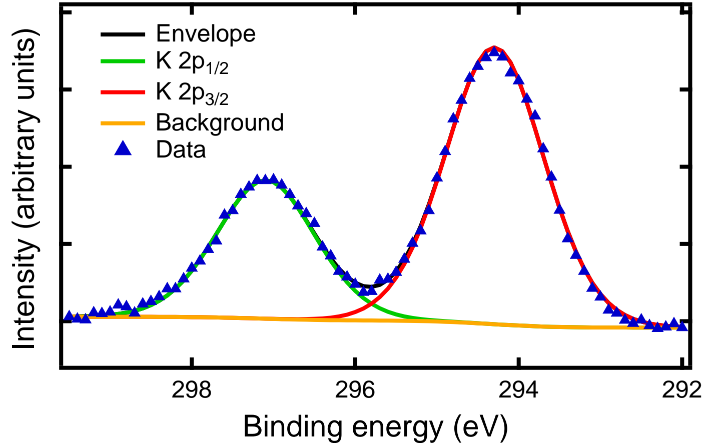

Figure 2.4: Example of fitted K $2p_{3/2}$ and K $2p_{1/2}$ core level peaks fitted with a Shirley background. The peaks were constrained such that the peak area of the K $2p_{1/2}$ was half of that of the K $2p_{3/2}$ peak with a binding energy 1.60 eV higher due to spin-orbit splitting, and with the full-width at half-maximum (FWHM) of both peaks the same.

electrons within a material [72]. Some ejected electrons interact with these electrons while travelling through the material towards the surface, causing losses of kinetic energy. For metals, this manifests itself in XPS spectra as a series of smaller peaks on the higher-binding energy side of core level peaks. For semiconductors, this effect is not usually observed due to their lower electron concentrations. However, for samples that exhibit strong electron accumulation, such as InN, the high carrier concentration close to the surface can cause plasmon loss features to appear, with the effect proportional to the electron concentration at the surface. These loss features are characterised by a series of peaks and as a tail on the high-binding energy side of core level peaks due to the varying, depth-dependent carrier concentration [73].

Valence band spectra

When looking at an XPS spectrum, the region with the lowest binding energy corresponds to electrons excited out of the valence band of a material. The intensity of this spectral region corresponds to the density of states (DOS) integrated across the Brillouin zone, and an example of this is shown in Figure 2.5. For metals, a Fermi step function is observed at the Fermi level, broadened

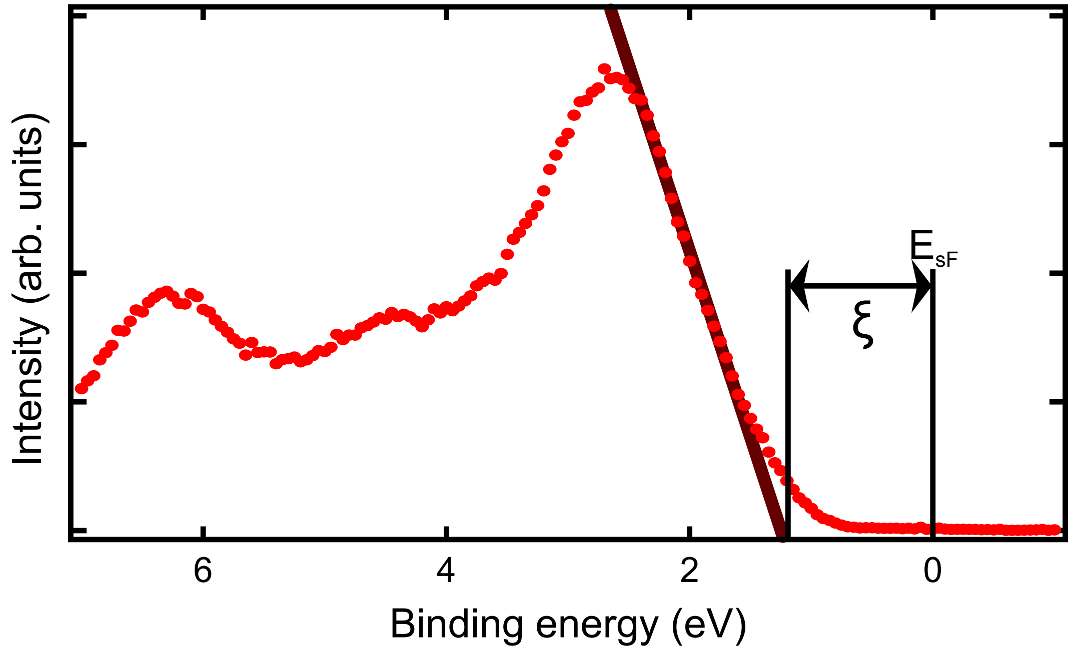

Figure 2.5: Valence band region of an XPS spectrum of an InN sample, showing ξ, the separation of the extrapolated valence band leading edge to the Fermi level at the surface, E_{sF}.

due to thermal effects. For semiconductors, the position of the leading edge of the spectrum (extrapolated, to account for the finite resolution of the spectrometer [74]) indicates the separation of the valence band maximum (VBM) and E_{sF}, the Fermi level at the surface. This separation is marked as ξ in Figure 2.5, and when compared to bulk measurements, can give information about surface band bending, as detailed in section 3.2. Calibration to determine the exact position of the Fermi level is essential, and the methodology is outlined in subsection 2.1.4.

Background

As can be seen from Figure 2.3, a step-like background is present in XPS spectra, which increases with increasing binding energy. This is due to inelastic scattering of photoelectrons which decreases their kinetic energy and gives them the appearance of having a higher binding energy. For peak fitting and analysis, a background subtraction is applied, with the Shirley model for XPS backgrounds being used throughout this thesis [75].

2.1.2 Chemical shifts

The observed binding energy is simply the energy difference between the n-electron initial state and the $(n-1)$-electron final state of the atom, minus the relaxation energy, $E_r(k)$, of the remaining electrons on the atom and of the surrounding atoms:

$$E_B = -\epsilon_k - E_r(k), \tag{2.2}$$

where ϵ_k is the orbital energy of the ejected photoelectron. Corrections for the differential correlation and relativistic energies also exist, but are typically small enough to be ignored [76]. If the initial state of the atom is changed, for example by chemical bonds with other atoms, the observed binding energy of the electrons in that atom will also change. This is called the chemical shift, ΔE_B. For most samples, ΔE_B can be adequately interpreted solely in terms of initial state effects, i.e.

$$\Delta E_B = -\Delta\epsilon_k. \tag{2.3}$$

Several examples of this correlation are given in the work by Siegbahn and colleagues [77]. However, caution must be used when solely attributing chemical shifts to initial state effects. Final state effects such as relaxation do not necessarily have a straightforward relationship with changes in the chemical environment and can have an impact on the measured binding energy. In principle, however, by fitting the core level peaks, it is possible to ascertain the bonding environments of the elements present through analysis of the binding energies of the peaks.

2.1.3 Quantification from XPS

As mentioned above, the area underneath the core level peaks is related to the quantity of the associated element present within the probing depth at the surface of the sample. After correcting for instrumental factors, by measuring the peak areas we can obtain the quantity of each element present. The equation commonly used for this is

$$I_{ij} \;=\; K\,T(KE)\,L_{ij}(\gamma)\,\sigma_{ij}\int n_i(z)\,e^{-z/\lambda(KE)\cos\theta}\,dz, \tag{2.4}$$

where I_{ij} is the area of peak j from element i, K is an experimental constant, $T(KE)$ is the transmission function of the analyser, $L_{ij}(\gamma)$ is the angular asymmetry factor for orbital j of element i, σ_{ij} is the photoionisation cross-section of peak j from element i, $n_i(z)$ is the concentration of element i at a distance z below the surface, $\lambda(KE)$ is the IMFP length, and θ is the take-off angle of the photoelectrons measured with respect to the surface normal. Usually, elemental percentages or ratios are required, meaning that it is not necessary to determine the absolute values of all of the quantities in Equation 2.4.

The instrumental constant, K, takes into account experimental parameters such as x-ray flux, sampling area and the acceptance angle of the analyser. These quantities are assumed constant over the time period required to acquire XPS spectra, and cancels when elemental ratios or percentages are calculated. For comparison of peak areas of spectra from different samples, careful normalisation of the background level removes differences in x-ray flux that may occur. Information about the efficiency of the collection lenses, analyser and detector of the XPS system comes is included in the transmission function. The variation of this function with KE comes from the retardation of the kinetic energy of the electrons as they pass through the lens system [78].

The angular asymmetry factor, $L_{ij}(\gamma)$, accounts for differences in the type of orbital and the angle γ between the incident x-rays and emitted photoelectrons (80° in this thesis). However, even where different types of orbitals are used for quantification, the variation in $L_{ij}(\gamma)$ is typically small. Where elemental ratios are calculated from peaks in this thesis, they are for comparison with the same peaks in other spectra taken using the same experimental setup, and so the angular asymmetry term is not required. The photoionisation constant σ_{ij} is the probability of a photoelectron from orbital j of element i being created by the incident x-ray. The values used throughout this thesis are taken from the calculations of Schofield [79].

The equations relating the IMFP, $\lambda(KE)$, to the electron energy and material the electron is travelling through have been developed by Seah and Dench [70], and the $\cos\theta$ term is to account for changes in sampling depth that occur as the take-off angle of the photoelectrons is changed. However, in this thesis, all XPS data was gathered with a take-off angle of 90° so the $\cos\theta$ term can be disregarded.

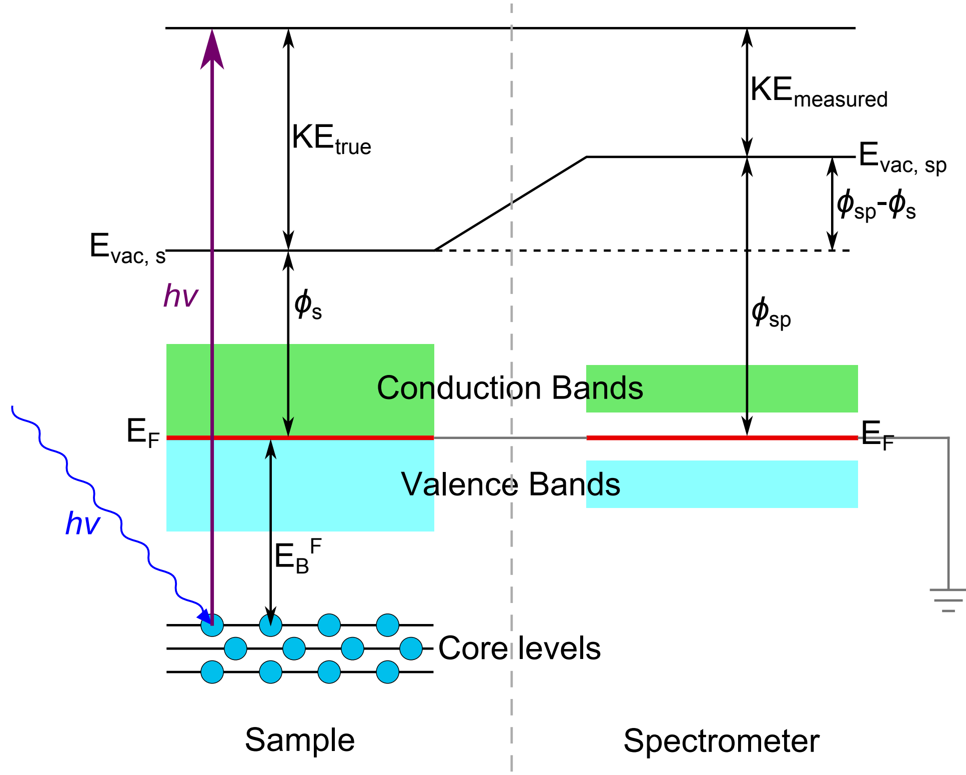

Figure 2.6: The energy level diagram for an electrically conducting sample that is grounded to the spectrometer. The Fermi levels of the sample and spectrometer are aligned ($E_f^s = E_f^{sp}$) so that E_B is referenced with respect to E_F. The measurement of E_B is independent of the sample work function, ϕ_s, but is dependent on the spectrometer work function, ϕ_{sp}.

2.1.4 Calibration

As shown in Figure 2.6, by placing a conducting sample in electrical contact with the spectrometer, the Fermi level of both the sample and spectrometer is positioned at the highest occupied energy level. Equation 2.1 then becomes

$$E_B^F = h\nu - KE - \phi_{sp}, \tag{2.5}$$

where E_B^F is E_B referenced to the Fermi level E_F, and ϕ_{sp} is the work function of the spectrometer. Therefore it is not necessary to know the work function of each sample analysed by XPS in order to know E_B^F. Throughout this thesis, the position of the Fermi edge for a clean polycrystalline silver reference sample

was used to determine the work function of the spectrometer. This took place a minimum of two days after the analyser electronics had been switched on, allowing time for the electronics to settle and removing any resultant drifting of ϕ_{sp}. Electrical contact between the InN samples and spectrometer was ensured by pressing tantalum foil or carbon tape, used to hold the sample in place, to a small area of the sample surface. The contact between the sample and the plate was then checked using a multimeter before samples were loaded into the UHV chamber.

2.1.5 Spectrometer

The XPS measurements in this thesis were conducted at the University of Warwick using an Omicron SPHERA concentric hemispherical analyser. The samples were probed using monochromated Al-K_α x-rays with a linewidth of 0.25 eV and the emitted photoelectrons were collected by an electrostatic hemispherical analyser comprising two concentric hemispheres with a mean radius of 125 mm. The spectrometer contained a large slit of 5 mm, and two sets of slits 3 mm and 1 mm wide for each of the 7 channeltrons. The effective instrumental resolution obtained from measuring the width of the Fermi edge of a clean polycrystalline silver sample is 0.33 eV at a pass energy of 5 eV, or 0.47 eV at a pass energy of 10 eV. This system operates in a chamber pumped by a turbomolecular pump, an ion pump and titanium sublimation pumps, and has a base pressure of $\sim 2\times10^{-11}$ mbar. The samples were held on a five axis manipulator and were mounted onto sample plates using carbon tape or tantalum foil spot-welded to the plate.

2.2 Hall effect measurements

The Hall effect was first observed by Edwin Hall in 1879 as a result of his investigations into a lack of consensus on the action of a magnet on a material carrying a current [80]. He observed that an electromotive force was induced perpendicular to the direction of current flow in the plane of a conducting film when placed in a magnetic field orientated such that the magnetic field lines were normal to the surface of the film. After further investigation this

potential was found to be proportional to the current and the magnetic field. With these measurements, it became possible for the first time to determine the sign of charge carriers in a conductor. These findings have led to the development of the single field Hall effect experiment which gives information about bulk carrier concentration and mobility. In semiconductors with an electron accumulation layer, such as InN, the carrier density will typically be overestimated due to the electrons from the accumulation being counted towards the average carrier density.

To perform the experiment, shown schematically in Figure 2.7, an electric field, E_x is applied to the sample and a current, I_x, flows through the semiconductor. A magnetic field, $\mathbf{B} = (0, 0, B_z)$, is applied, and an electric field is generated perpendicular to the direction of current flow by the Lorentz force [81]. As the charge carriers accumulate at the edge of the sample, an electric field builds up that opposes their motion. At equilibrium, this electric (Hall) field, E_y, satisfies the relations

$$\frac{ev_{ey}}{\mu_e} = eE_y + ev_{ex}B_z \tag{2.6a}$$

$$\frac{ev_{hy}}{\mu_h} = eE_y - ev_{hx}B_z, \tag{2.6b}$$

where v_{ey} (v_{hy}) is the electron (hole) drift velocity along y, and μ_e (μ_h) is the electron (hole) drift mobility. Because $v_{ex} = \mu_e E_x$ and $v_{hx} = \mu_h E_x$, these can

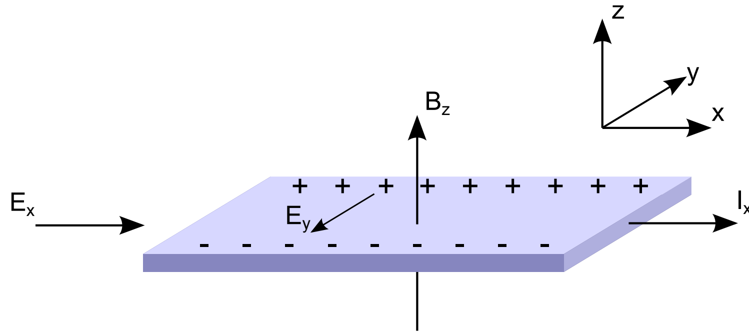

Figure 2.7: Schematic of Hall's experiment. As the current I_x flows through the sample in the magnetic field, B_y, the Lorentz force acts to deflect the charge carriers to the sides of the block, which creates the Hall field, E_y.

be substituted into Eqs. 2.6 to give the following expressions:

$$\frac{v_{ey}}{\mu_e} = E_y + \mu_e E_x B_z \tag{2.7a}$$

$$\frac{v_{hy}}{\mu_h} = E_y - \mu_h E_x B_z. \tag{2.7b}$$

As Ohm's law states, $I = JA$, where J is the current density and A is the cross-sectional area, then $I_y = I_e + I_h$. If we assume that in the y-direction there is no current flow, then

$$J_y = J_{ey} + J_{hy} = env_{ey} + epv_{hy} = 0 \tag{2.8}$$

and therefore

$$nv_{ey} = -pv_{hy}, \tag{2.9}$$

where n (p) is the electron (hole) density. The current density in the x-direction is given by

$$J_x = (p\mu_e + n\mu_h)eE_x. \tag{2.10}$$

Bringing together Eqs. (2.7), (2.9) and (2.10), the following expression is obtained:

$$eE_y(n\mu_e + p\mu_h)^2 = B_z J_x(p\mu_h^2 - n\mu_e^2). \tag{2.11}$$

From this the Hall coefficient, $R_H = E_y/J_x B_z$, may be obtained. With both electrons and holes present, this is given by

$$R_H = \frac{1}{|e|}\frac{(p\mu_h^2 - n\mu_e^2)}{(n\mu_e + p\mu_h)^2}. \tag{2.12}$$

2.2.1 Van der Pauw Geometry

In 1958, L. J. van der Pauw described a geometry which can be used to obtain the resistivity, doping type, sheet carrier density and mobility of the majority carrier of a sample [82], as illustrated in Figure 2.8. With the contacts at points a, b, c and d, a current I_{ab} can be applied from contact a to b, and a voltage, V_{cd}, can be measured between contacts c and d. If the current and voltage are then measured in the perpendicular directions, two characteristic

resistances, $R_{ab,cd}$ and $R_{ad,bc}$ are given by

$$R_{ab,cd} = \frac{V_{cd}}{I_{ab}} \quad R_{ad,bc} = \frac{V_{bc}}{I_{ad}}. \tag{2.13}$$

The van der Pauw equation,

$$\exp(-\pi R_{ab,cd}/R_s) + \exp(-\pi R_{ad,bc}/R_s) = 1, \tag{2.14}$$

relates the characteristic resistances to the sheet resistance, R_s. The measurements can be made more accurate by also measuring the current and voltage along the parallel edges, and by repeating the measurements with reversed polarity, thus obtaining average values for the characteristic resistances. The resistivity of the sample is simply R_s multiplied by the thickness of the sample.

To obtain the overall Hall voltage, measurements must be made with a magnetic field applied in both the positive and negative z-directions. Measurements made in the positive (negative) direction will be indicated by a superscript + (−). The current is applied in across the diagonals of the sample in turn, taking advantage of reversing the polarity, with the voltage, e.g. V_{13}^{+}, measured for each current. The magnetic field is then reversed and the

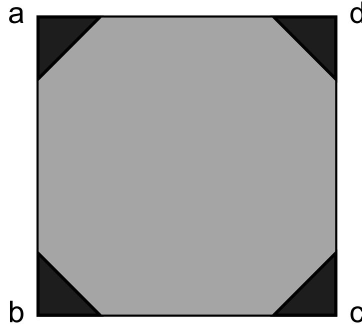

Figure 2.8: Plan view of the van der Pauw geometry used for single field Hall effect measurements. Metal contacts are placed at positions a, b, c and d enabling current to be passed between the contacts and measurements of voltage to be made.

measurements repeated. The overall Hall voltage is then given by

$$V_H = \frac{V_{13}^+ + V_{24}^+ + V_{31}^+ + V_{42}^+ - (V_{13}^- + V_{24}^- + V_{31}^- + V_{42}^-)}{8} \tag{2.15}$$

The Hall voltage can be defined by

$$V_H = \frac{IB}{en_s}, \tag{2.16}$$

where n_s is the sheet density of the charge carrier. Combining Eqs. (2.15) and (2.16), the electron density can be found by multiplying n_s by the thickness of the sample, with a positive (negative) sign indicating the material is p-type (n-type).

Ecopia HMS-3000 system

All Hall effect measurements made in this thesis were made using the Ecopia HMS-3000 system. The magnetic field strength used was 0.55 T, and the polarity of the magnetic field was changed by rotating the magnet 180°. The Van der Pauw geometry was used and all measurements were made at room temperature. Measurements of current and voltage can be taken between each of the contacts, and the system can pass a current of up to 20 mA.

Chapter 3

Theoretical Methods

This chapter outlines the theoretical calculations which form the basis of investigating the surface electronic properties of InN. The band bending and charge carrier concentration profile at the surface were calculated by solving Poisson's equation incorporating a modified Thomas-Fermi approximation (MTFA), as developed by Paasch and Übensee [83]. InN exhibits a non-parabolic band dispersion, so Kane's **k·p** approximation [84] is used to model the conduction band dispersion. At the surface, an infinite potential step is assumed, and modifications are made to the local density of states to approximate the effects of quantum-mechanical reflection at this barrier, which is then extended to incorporate the non-parabolicity of the conduction band [85]. The correction factor in the MTFA physically represents the interference of incident and reflected electron wave functions due to the potential barrier at the surface.

3.1 Band structure approximations

3.1.1 Parabolic approximation

For many semiconductors it is sufficient to simply consider a parabolic dispersion of the valence and conduction bands ($E_v(k)$ and $E_c(k)$ respectively) around Γ in the Brillouin zone, as the extrema of the valence and conduction bands are located here for most semiconductors. This is given by

$$E_v(k) = E_v(0) - \frac{\hbar k^2}{2m_h^*} \tag{3.1a}$$

and

$$E_c(k) = E_c(0) + \frac{\hbar k^2}{2m_0^*}, \tag{3.1b}$$

where k is the wavevector and m_h^* and m_0^* are the hole and electron effective masses respectively.

This approximation, however, is only applicable to semiconductors with a large band gap. In the case of InN, a stronger interaction occurs between the valence and conduction bands due to the narrow band gap, and since a large occupation of the conduction band and non-parabolicity of the bands cannot be ignored, Equation 3.1b cannot be used in that form.

3.1.2 k.p perturbation theory

Quasi-particle corrected density functional theory (QPC-DFT) calculations of the InN bulk band structure across the Brillouin zone (Figure 1.9) have shown that the upper three bands exhibit p-orbital symmetry and are strongly influenced by a non-parabolicity near Γ [47]. The conduction band is highly non-parabolic with s-orbital symmetry and the higher conduction bands have little influence on the dispersion around the conduction band minimum (CBM) due to their large energy separation. This suggests that the $\mathbf{k}\cdot\mathbf{p}$ approach developed by Kane for the zinc-blende structure of InSb [84] described below is a reasonable approximation of the InN band structure around Γ. In this approximation the momentum operator (Equation 1.3) and magnetic effects (V_{so} and V_{cr} for spin-orbit and crystal field splitting respectively) are included. Using Bloch's theorem for waves in a periodic potential, described in subsection 1.4.1, the one-electron Schrödinger equation can be written as

$$\left[\hat{H}_0 + \frac{\hbar}{m}\mathbf{k}\cdot\mathbf{p} + V_{so} + V_{cr}\right] u_{\nu\mathbf{k}}(\mathbf{r}) = \tilde{E}_{\nu\mathbf{k}}(\mathbf{r}) u_{\nu\mathbf{k}}(\mathbf{r}). \tag{3.2}$$

Here $\hat{H}_0 = \frac{\mathbf{p}^2}{2m} + V_0(\mathbf{r})$ and $\tilde{E}_{\nu\mathbf{k}}(\mathbf{r}) = E_v(\mathbf{k}) - \frac{\hbar^2 k^2}{2m}$. At the Γ-point ($\mathbf{k} = (0,0,0)$), Equation 3.2 reduces to

$$\left[\hat{H}_0 + V_{so} + V_{cr}\right] u_{\nu\mathbf{0}}(\mathbf{r}) = \tilde{E}_{\nu\mathbf{0}}(\mathbf{r}) u_{\nu\mathbf{0}}(\mathbf{r}), \tag{3.3}$$

the solutions of which form an orthonormal set. From here, the **k·p** interaction between the valence and conduction bands can be treated as a perturbation in order to express the energy eigenvalues and the wavefunction of any point near the Γ-point in **k**-space.

In Kane's **k·p** approximation the Hamiltonian describing interaction between the three highest valence bands and the conduction band is given by

$$H = \begin{bmatrix} \hat{H} & 0 \\ 0 & \hat{H} \end{bmatrix}, \tag{3.4a}$$

where

$$\hat{H} = \begin{bmatrix} E_s & 0 & kP & 0 \\ 0 & E_p - \Delta_{so}/3 & \sqrt{2}\Delta_{so}/3 & 0 \\ kP & \sqrt{2}\Delta_{so}/3 & E_p & 0 \\ 0 & 0 & 0 & E_p + \Delta_{so}/3 \end{bmatrix}. \tag{3.4b}$$

$E_s(E_p)$ is the conduction (valence) band edge energy, Δ_{so} is the spin-orbit splitting and $P \equiv \langle u_s|\mathbf{p}|u_i\rangle$ is Kane's matrix element, with $u_{s,i}$ the Bloch lattice-functions possessing the s- and p_i-orbital symmetries ($i = x, y, z$). In InN, Δ_{so} is ~5 meV ($\ll E_g$) and can be neglected, reducing the Hamiltonian to

$$H = \begin{bmatrix} E_s & kP \\ kP & E_p \end{bmatrix}. \tag{3.5}$$

The crystal field splitting and effective mass anisotropy in InN are small, so the conduction band dispersion is adequately described when the material is assumed to be isotropic and have no crystal field splitting. The conduction band dispersion is described by

$$E_c(k) = E' + \frac{\hbar^2 k^2}{2m_0}. \tag{3.6}$$

Here m_0 is the free electron mass and E' is the largest eigenvalue of the Hamiltonian given in Equation 3.4, which is given by the largest solution to

$$E'(E' + E_g) - k^2P^2 = 0, \tag{3.7}$$

where $E_s = 0$ and $E_p = -E_g$ have been used, defining the energy as zero at

the CBM. Kane's matrix element is given by

$$P^2 = \frac{\hbar^2}{2m_0}\left(\frac{m_0}{m_0^*} - 1\right) E_g, \tag{3.8}$$

with m_0^* being the conduction band effective mass. Solving Equation 3.7 and substituting into Equation 3.6, the two-band **k·p** analytic form for the conduction band dispersion is

$$E_c(k) = \frac{1}{2}\left[-E_g + \sqrt{E_g^2 + 4k^2P^2}\,\right] + \frac{\hbar^2 k^2}{2m_0}, \tag{3.9}$$

and the density of conduction band states is given by

$$g_c(k) = \frac{k^2}{\pi^2}\left[\frac{dE_c(k)}{dk}\right]^{-1} = \frac{k\pi^{-2}}{2P^2[E_g^2 + 4k^2P^2]^{-\frac{1}{2}} + \left(\frac{\hbar^2}{m_0}\right)}. \tag{3.10}$$

Using Equations (3.9) and (3.10), the density of states as a function of energy can be obtained, allowing the number of filled states to be determined for a given Fermi level.

3.2 Poisson's equation

The band bending in the space charge region is described by the one-electron potential, $V(z)$, as a function of depth z below a semiconductor surface. This must satisfy Poisson's equation

$$\frac{d^2V}{dz^2} = -\frac{e}{\epsilon(0)\epsilon_0}[N_D^+ - N_A^- - n(z) + p(z)], \tag{3.11}$$

where e is the electron charge, $\epsilon(0)$ is the static dielectric constant, ϵ_0 is the permittivity of vacuum, N_D^+ (N_D^-) is the bulk donor (acceptor) density, assumed constant throughout the semiconductor, and $n(z)$ [$p(z)$] is the electron (hole) density. Because the calculations were made for n-type InN with electron accumulation at the surface, N_D^- and $p(z)$ can be taken to be 0. To satisfy charge neutrality, there can be no band bending in the bulk of the

semiconductor, therefore $V(z)$ must satisfy the boundary condition

$$V(z) \to 0 \text{ as } z \to \infty. \tag{3.12}$$

Also,

$$\left.\frac{dV}{dz}\right|_{z=0} = \frac{e}{\epsilon(0)\epsilon_0} N_{ss}, \tag{3.13}$$

where N_{ss} is the surface state density. The total band bending at the surface, V_{bb}, can therefore equivalently be considered as a boundary condition. This can be determined from valence band XPS spectra, as detailed in section 2.1.1, in conjunction with Hall effect measurements (subsection 2.2.1). The VBM to Fermi level separation at the surface, ξ, is measured in XPS and the position of the Fermi level relative to the CBM in the bulk, E_F^{CB}, is given by numerically solving

$$N_b = \int_0^\infty g_c(E) f_{FD} dE \tag{3.14}$$

where N_b is the bulk charge carrier density, given by Hall effect measurements, and f_{FD} is the Fermi-Dirac distribution

$$f_{FD}(E) = \frac{1}{1 + exp\left\{\frac{1}{k_B T}[E - E_F^{CB}]\right\}}. \tag{3.15}$$

Here, k_B is Boltzmann's constant and T is temperature. The VBM to Fermi level separation in the bulk is then $(E_g + E_F^{CB})$ and the total band bending is simply given by

$$V_{bb} = \xi - (E_g + E_F^{CB}), \tag{3.16}$$

as illustrated in the example of numerically calculated band bending given in Figure 3.1.

3.2.1 Modified Thomas-Fermi approximation (MTFA)

Poisson's equation (Equation 3.11) must be solved self-consistently with the one-electron Schrödinger equation (Equations (1.1) and (1.5)) in order to obtain the potential $V(z)$ and the charge carrier density profile. However, this problem is highly non-linear due to the dependence of the carrier concentra-

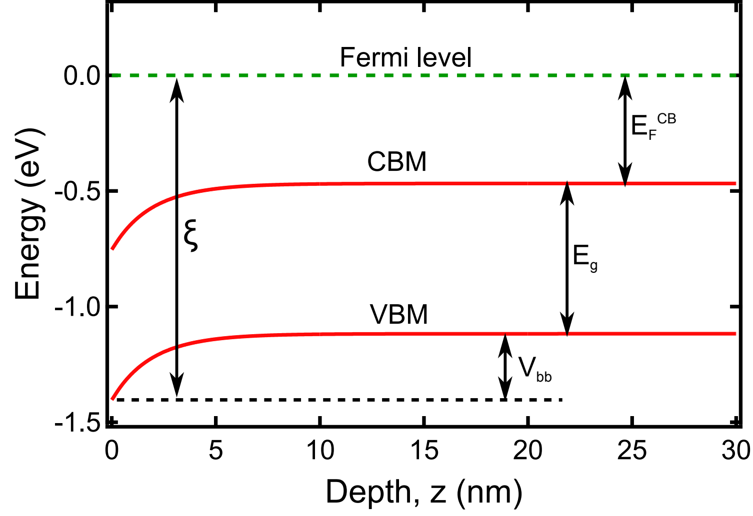

Figure 3.1: Example of band bending of the CBM and VBM at an InN surface as calculated numerically from experimentally determined values for the valence band–Fermi level separation, ξ, the bulk charge carrier concentration and the valence band bending, V_{bb}. The band bending is caused by the presence of unoccupied donor-like surface states.

tions in Equation 3.11 on the potential. The problem is simplified using a modified Thomas-Fermi approximation as developed by Paasch and Übensee [83], which has been shown to yield band bending and charge carrier concentration profiles in good agreement with those obtained through fully self-consistent Poisson-Schrödinger calculations. This approximation has also been compared with experiment for narrow gap depletion and accumulation layers for InSb and InAs respectively [86, 87], as well as for InN [85].

In this approach, the one-electron potential is calculated within the MTFA subject to the boundary conditions with carrier density calculated from

$$n(z) = \int_0^\infty g_c(E) f_{FD} f(z) dE \; , \qquad (3.17)$$

corresponding to the conduction band, where g_c is the density of states for the non-parabolic conduction band given in Equation 3.10, f'_{FD} is the Fermi-Dirac

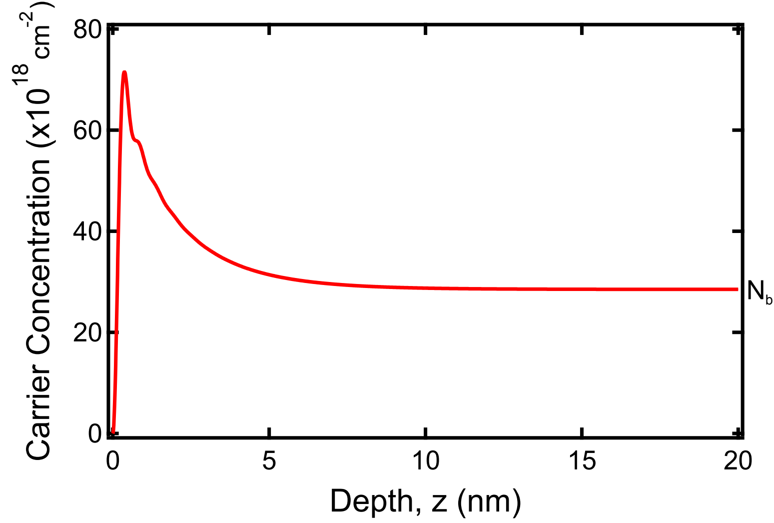

Figure 3.2: Example of numerically calculated charge carrier concentration profile at an InN surface, showing the existence of an electron accumulation layer within the top 5 nm before decreasing until the bulk charge carrier concentration, N_b, is reached.

function including the potential dependence

$$f'_{FD}(E) = \frac{1}{1 + exp\left\{\frac{1}{k_B T}[E - E_F^{CB} + V(z)]\right\}}, \tag{3.18}$$

and $f(z)$ is the MTFA factor accounting for the potential barrier at the surface,

$$f(z) = 1 - \text{sinc}\left[\frac{2z}{L}\left(\frac{E}{k_B T}\right)^{\frac{1}{2}}\left(1 + \frac{E}{E_g}\right)^{\frac{1}{2}}\right]. \tag{3.19}$$

Here $L = \hbar/(2m_0^* k_B T)^{1/2}$ is the thermal length for non-degenerate semiconductors, and $L = \frac{1}{k_F}$ is the Fermi length for degenerate semiconductors. A semiconductor is considered non-degenerate if the Fermi level lies in the band gap and is more than $3k_B T$ from either of the band edges. The Fermi level in InN lies above the CBM, therefore making it a degenerate semiconductor, and although the length scale is comparable to the depth of the accumulation layer, experiment has shown good agreement with this approximation [85].

The numerical solutions to Poisson's equation and to $n(z)$ can be found by using a trial solution, and then by using interval bisection to converge on the

band bending potential which satisfies the boundary conditions. An example of the calculated $n(z)$ for an InN sample is shown in Figure 3.2. It can be seen that the charge carrier concentration is effectively bulk-like at depths greater than 10 nm, which closely matches the probing depth of XPS making it a good tool for investigating electron accumulation. The kink visible at ~1 nm is due to the correction factor in the MTFA.

In summary, the theoretical methods outlined in this chapter, used in conjunction with XPS and Hall effect measurements, allow the investigation of the effect of surface treatments on the band bending and charge carrier concentration profiles at semiconductor surfaces.

Chapter 4

Ex-situ Sulfur Treatment of InN Surfaces

4.1 Introduction

Studies into passivation and electron accumulation reduction at InN surfaces have previously focussed on immersing samples in $(NH_4)_2S_x$ solution ex-situ, after having previously etched the sample in HCl and rinsed it in deionised water [66–68]. This cleaning process still permits the re-oxidation of the surface between etching and sulfur treatment, with the possible introduction of contaminants and a reduction in the effectiveness of treatment. Therefore it is desirable to develop a treatment process which both etches and passivates the surface at the same time.

For these experiments, disulfur dichloride (S_2Cl_2) solution was used, with the hypothesis that the chlorine would etch the sample and the sulfur would simultaneously form bonds to lower the surface Fermi level and passivate the surface, thus removing the exposure to atmosphere between the etching and treatment. Chlorine is also highly electronegative (3.16 on the Pauling scale) and would help to draw electrons from the accumulation layer, as seen in the work of King et. al. [73], however, it is less thermally stable than sulfur at the surface of indium nitride.

4.2 Experimental Details

In these experiments, an n-type In-polar c-plane InN wafer grown by Veeco Instruments Inc. using plasma assisted molecular beam epitaxy (PAMBE) was used. Hall effect measurements revealed a charge carrier concentration of 2.0×10^{18} cm^{-3}, and using the calculations outlined in section 3.2, this corresponds to a Fermi level position 0.1 eV above the CBM. Initial XPS measurements showed a valence band-Fermi level separation of ξ =1.32±0.05 eV, indicating an initial band bending of 0.57±0.05 eV. Pieces of the InN wafer were then immersed in the S_2Cl_2 solution for 1 minute and 6 minutes respectively, before being blown dry in N_2 gas and immediately affixed to a sample plate using carbon tape to reduce transfer time before being transferred into the UHV vacuum system for analysis.

4.3 Results and Analysis

The valence band spectra for the samples treated for 1 minute and 6 minutes both showed a shift in the position of the valence band leading edge to lower binding energies, shown in Figure 4.1, indicating that the treatment was effective in reducing the surface Fermi level. However, the greater shift occurred for the sample treated for 1 minute, indicating a loss of effectiveness for longer treatment times. For the sample that was immersed for 1 minute, the valence band region showed a reduction in ξ of 0.19±0.05 eV. Using the theoretical calculations outlined in chapter 3, this corresponded to a reduction in electron accumulation of ~53 %. For the sample immersed for 6 minutes, the reduction in ξ, and therefore band bending, was slightly smaller, only 0.16±0.05 eV, and the reduction in electron accumulation was ~44 %. The band bending and charge carrier concentration profiles are shown in Figure 4.2.

Looking at the S 2p region of the XPS spectra, it should be possible to analyse the bonding configurations of sulfur atoms at the surface of the samples, and these are shown in Figure 4.3. For the sample immersed in the S_2Cl_2 solution for 1 minute, three doublet peaks are observed with the S $2p_{3/2}$ peaks at 161.6 eV (S1), 163.5 eV (S2) and 167.8 eV (S3). S1 is assigned to an In–S–S–In bonding environment, using the work of Hyland

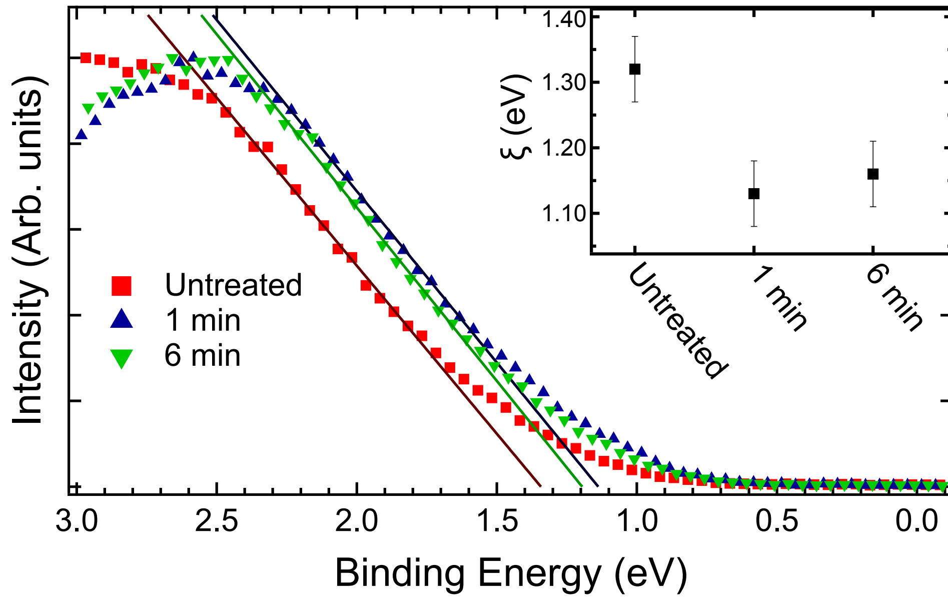

Figure 4.1: Normalised valence band region for the untreated and S_2Cl_2 treated InN samples and (inset) changes in the separation of the surface Fermi level position from the valence band leading edge (ξ). The sample treated for 6 minutes showed a lesser reduction in ξ than for 1 minute treatment.

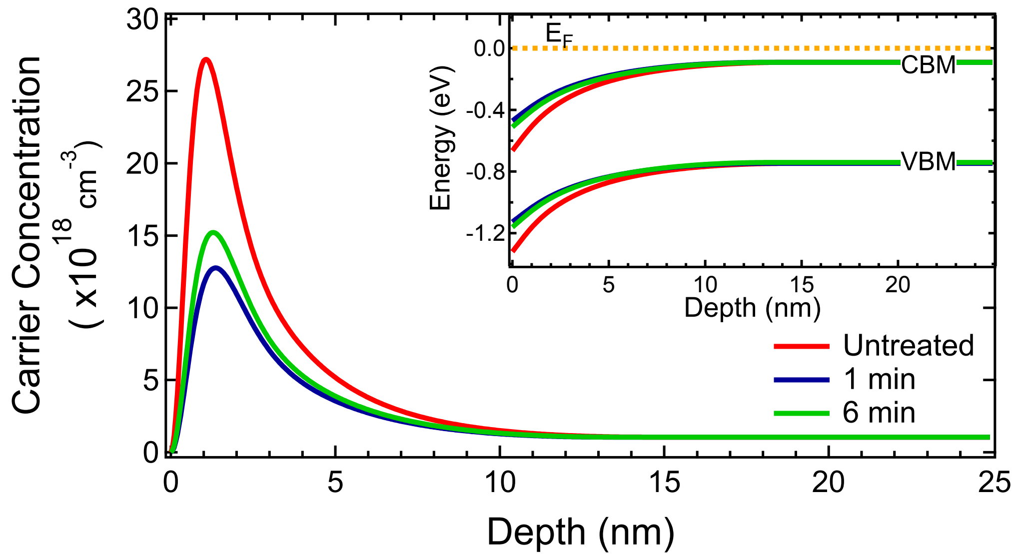

Figure 4.2: Charge carrier concentration and (inset) band bending profile for the untreated sample (red) and those treated for one minute (blue) and six minutes (green).

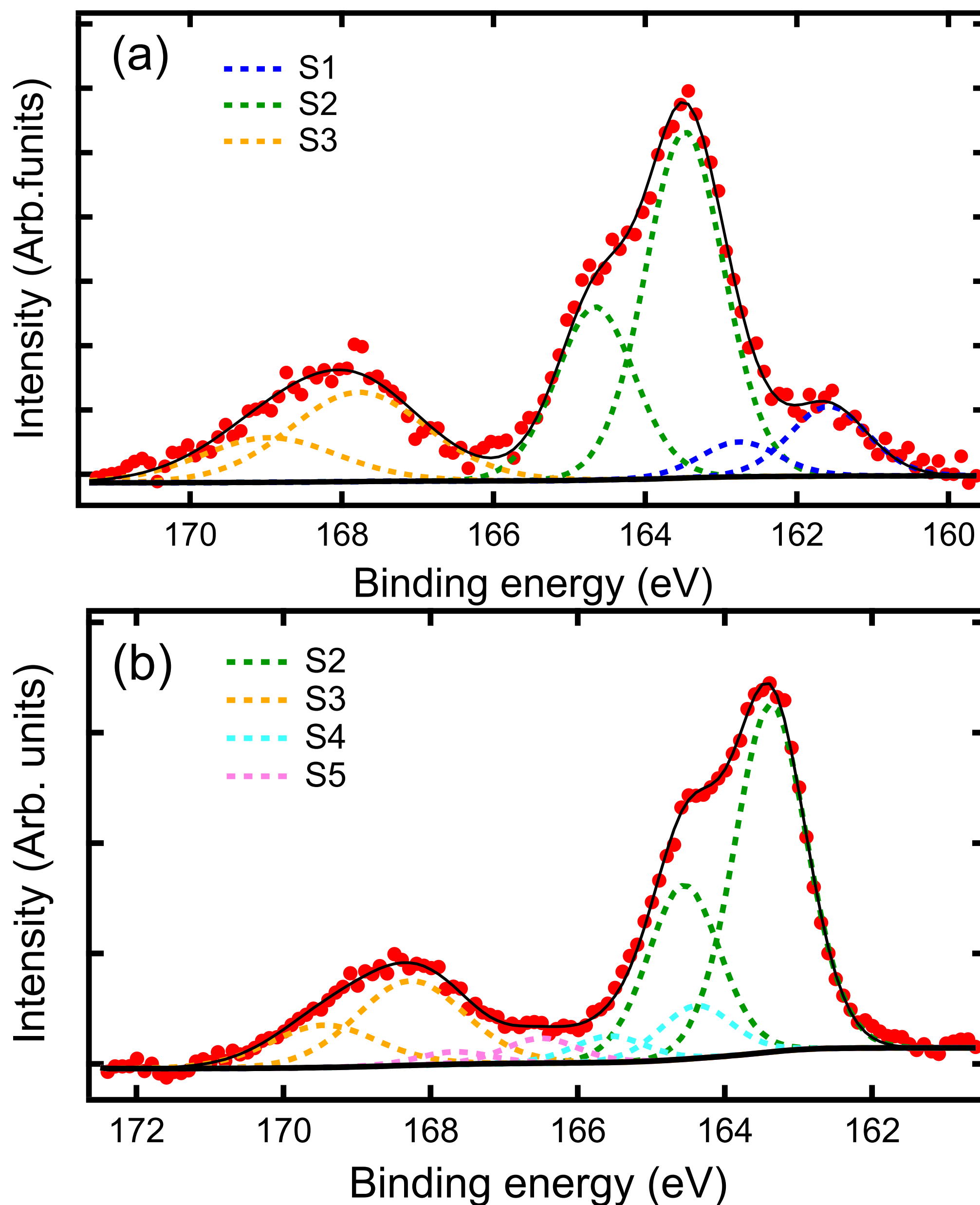

Figure 4.3: XPS data showing the S 2p region of the sample immersed in S_2Cl_2 for (a) 1 minute and (b) 6 minutes. The sample immersed for 6 minutes shows the presence of additional sulfur bonding configurations and the absence of the doublet at 161.6 eV. Peak assignments are given in the main text. Additional doublet peaks in (b), S4 and S5, were fitted because the shoulder at ~164.4 eV is too intense to be from the S $2p_{1/2}$ peak of S2 (the area of a $2p_{1/2}$ peak must be half of that of the corresponding $2p_{3/2}$ peak as explained in section 2.1.1) and the shape of the spectra at 165.5 eV is flatter and more intense than in (a).

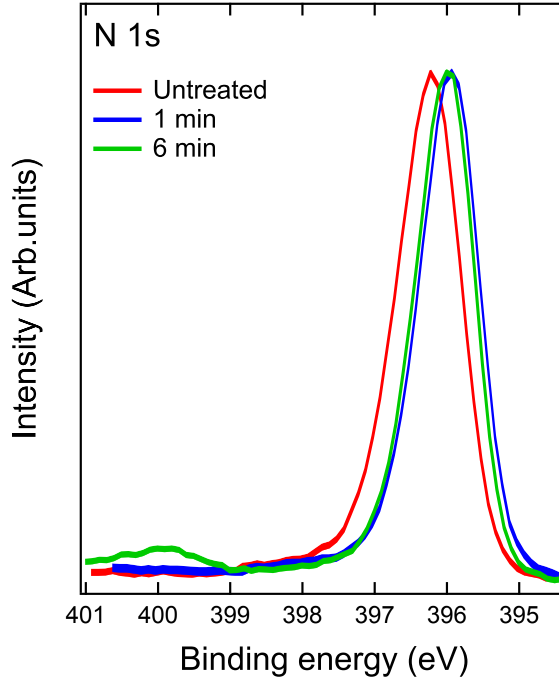

Figure 4.4: Normalised N 1s region the untreated and S_2Cl_2 treated InN samples, showing the presence of a peak at ~400 eV for the sample treated for 6 minutes indicating that the solution has etched through the adlayers.

and Bancroft as a guide to sulfur-metal bonding peak binding energies [88]. S2 is characteristic of elemental sulfur on the surface and also to the S_2Cl_2 molecule, and S3 can be assigned to SO_2 or $SOCl_2$. The sample treated for 6 minutes has a very different S 2p region, with doublet peaks at 163.4 eV (S2), 164.4 eV (S4), 166.5 eV (S5) and 168.3 eV (S3). S2 is again attributed to elemental sulfur or S_2Cl_2 at the surface and S3 to SO_2 or possibly $SOCl_2$. Unlike for the sample immersed for one minute, this S 2p has no component corresponding to an environment where sulfur is bonded to indium and there are two additional doublet peaks that were not previously observed. S4, at 164.4 eV, is characteristic of S_2N_2 [89], indicating that the chlorine may have etched the indium adlayers and exposed the nitrogen atoms underneath. The peak at 166.5 eV, S5, may then correspond to another nitrogen containing molecule, though it is possible that the peak is not necessary for fitting the data.

The idea that the In adlayers have been etched through by the chlorine

is supported by analysis of the N 1s region, shown in Figure 4.4, where a peak at ~400 eV is only present on the sample etched for 6 minutes. Drawing analogy from sulfur treatment of InAs, this may explain the less significant reduction in ξ for the sample treated for 6 minutes. The etching of the adlayers allows sulfur atoms to occupy the group V sublattice, thereby acting as a donor and increasing band bending [63, 64]. The N 1s region also shows a shift to lower binding energy for the samples treated with S_2Cl_2, with the greatest shift observed on the sample treated for 1 minute. This is due to the reduction in ξ, with the entire spectrum shifted to lower binding energies. For the sample treated for 1 minute this shift is 0.18±0.05 eV, and for the sample treated for 6 minutes the shift is 0.16±0.05 eV. These values closely match the values obtained for the change in ξ by extrapolating the leading edge of the valence band region.

The elemental ratios of nitrogen and indium were calculated from the XPS spectra of the N 1s and In 3d peaks using the methodology outlined in subsection 2.1.3, giving N to In ratios of 35:65, 33:67, and 32:68 for the untreated, 1 minute and 6 minute treated samples respectively. The error in these calculations is approximately ±5 %, so it cannot be said from this data whether the indium is being etched away. The probing depth of XPS is approximately 10 nm, however the thickness of the In-adlayers is <2 nm, meaning that there is a large contribution from the stoichiometric InN below that may mask any small changes in the amount of indium. In order to investigate this further, measurements with varying take-off angle would be required in order to increase the surface sensitivity.

In the O 1s region shown in Figure 4.5, the components at 530 eV, 532 eV and 533.1 eV are labelled as O1, O2 and O3 respectively. Peak O1 is assigned to In_2O_3, O2 to $In(OH)_3$ and O3 to adventitious atomic oxygen, using the binding energy values determined by Nefedov et al. [90] and Wagner et al. [91]. It can be seen that although the 6 minute treatment removed the In_2O_3 component, after only 1 minute of treatment this component appears to be larger than for the untreated sample. The component corresponding to $In(OH)_3$ decreases for both treatment times by a similar amount, so it is speculated that for the 1 minute treatment, the hydrogen atoms have been removed, allowing more In_2O_3 to form. The adventitious atomic oxygen com-

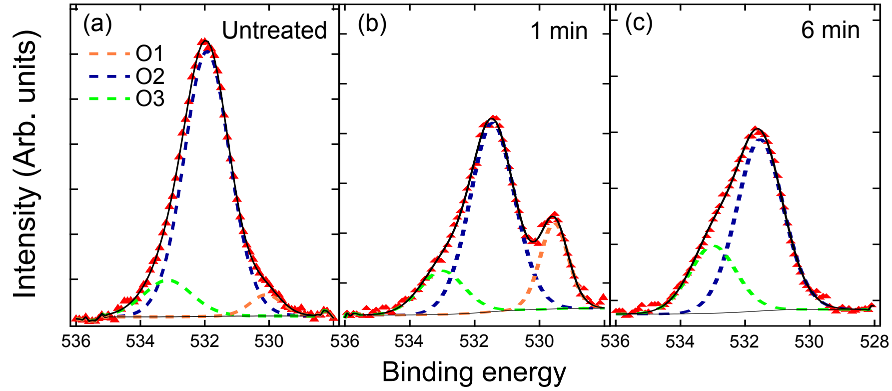

Figure 4.5: O 1s region for the (a) untreated sample and the samples immersed for (b) 1 minute and (c) 6 minutes in S_2Cl_2 solution, showing the growth of the component labelled O1 after 1 minute of treatment and its absence for the sample treated for 6 minutes. The assignments for the component peaks are given in the main text.

ponent remains throughout, even seemingly becoming larger for the sample treated for 6 minutes, though this may be due to slight differences in loading times between treatment and entry into the vacuum chamber.

4.4 Conclusions

These experiments investigated a new method of sulfur treatment using S_2Cl_2 solution to concurrently etch and passivate the InN surface. A large reduction in electron accumulation was observed for the sample treated for one minute, however this reduction decreased for the sample treated for 6 minutes due to etching through the In adlayers. This etching effect was observed through analysis of the S 2p and N 1s regions of the XPS spectra. It was also observed that the solution failed to remove a significant fraction of the indium oxide components, possibly due in part to the fact that the etched adsorbates remain in the solution throughout the treatment. It was at this point that the decision was made to investigate sulfur treatment of InN surfaces in-situ in order to have much greater control and understanding of the interaction of sulfur atoms at the surface.

Chapter 5

In-situ Sulfur Deposition on InN Surfaces

5.1 Introduction

As discussed in detail in section 1.6, several recent studies [66, 67] have shown that the use sulfur is effective in reducing the electron accumulation layer at the surface. This is due to the high electronegativity of sulfur [62], such that when it forms bonds with indium, charge is transferred to the sulfur atoms and the indium adlayers at the surface prevent the substitution of sulfur onto nitrogen sites. This is in contrast to the effect of sulfur on indium arsenide, where sulfur acts as a donor and enhances band bending due to sulfur being substituted on the group V sublattice [64, 92]. To date, experiments on the reduction of surface electron accumulation on InN surfaces have focussed on ex-situ methods of sulfur deposition on the surface, such as immersing the sample in $(NH_4)_2S_x$ solution [54, 66, 68]. The ex-situ nature of the immersion creates difficulties in accurate control of the rate of sulfur adsorption on the surface, and limiting contamination during this process is also troublesome. With an in-situ deposition method, it should be possible to perform controlled sulfur deposition experiments on clean InN surfaces. Deposition rates can be finely controlled using a well calibrated system in order to achieve consistent results. The structure and electronic properties of the treated surface can then be studied under UHV conditions without any contamination of the surface

occurring.

This chapter reports on the high-resolution XPS measurements of an a-plane InN sample and an In-polar c-plane InN sample during in-situ sulfur deposition from an electrochemical cell. For the c-plane InN sample, this was carried out with the sample held at a raised temperature in an attempt to increase the sulfur coverage [93]. Using valence band XPS data as described in section 2.1.1, band bending and charge profile calculations for these samples (made by numerically solving the Poisson-Schrödinger equation within the MTFA, as outlined in subsection 3.2.1) show that the surface separation of the VBM and Fermi level of InN decreases as sulfur is deposited, leading to near-flat bands at the surface. Analysis of other core level peaks in the XPS spectrum support the conclusion that a large reduction in electron accumulation has been achieved, while also shedding light on the various interactions of sulfur on these surfaces.

5.2 Experimental details

The samples used were grown by PAMBE at Cornell University, USA, by W. J. Schaff and Hai Lu, and at the University of California, Santa Barbara, USA, by J. S. Speck and members of his research group. The a-plane sample was grown to a thickness of 1000 nm, and the In-polar c-plane sample was grown to be 100 nm thick. Details of the growth process can be found elsewhere [94]. Hall effect measurements determined the charge carrier densities to be 2.85×10^{19} and 2.3×10^{18} cm^{-3} with electron mobilities of 2.04×10^{2} cm^{2}/Vs and 1.12×10^{3}cm ^{2}/Vs for the a-plane and c-plane samples respectively, though this may slightly overestimate bulk electron concentrations due to the surface electron accumulation layer. The samples were prepared by etching in 30 % HCl solution for 90 seconds before being immediately blown dry in N_2 gas, mounted on a sample plate and loaded into vacuum. Total transfer time between etching and loading into the chamber was no more than 5 minutes. The samples were then annealed to 320 °C for 2 hours. As can be seen from Figures 5.1 and 5.2(a), this removed nearly all of the carbon, oxygen and chlorine from the surface, including the oxide component of the In 3d peaks, (Figure 5.2(b)). A sharp (1×1) low energy electron diffraction (LEED) pattern

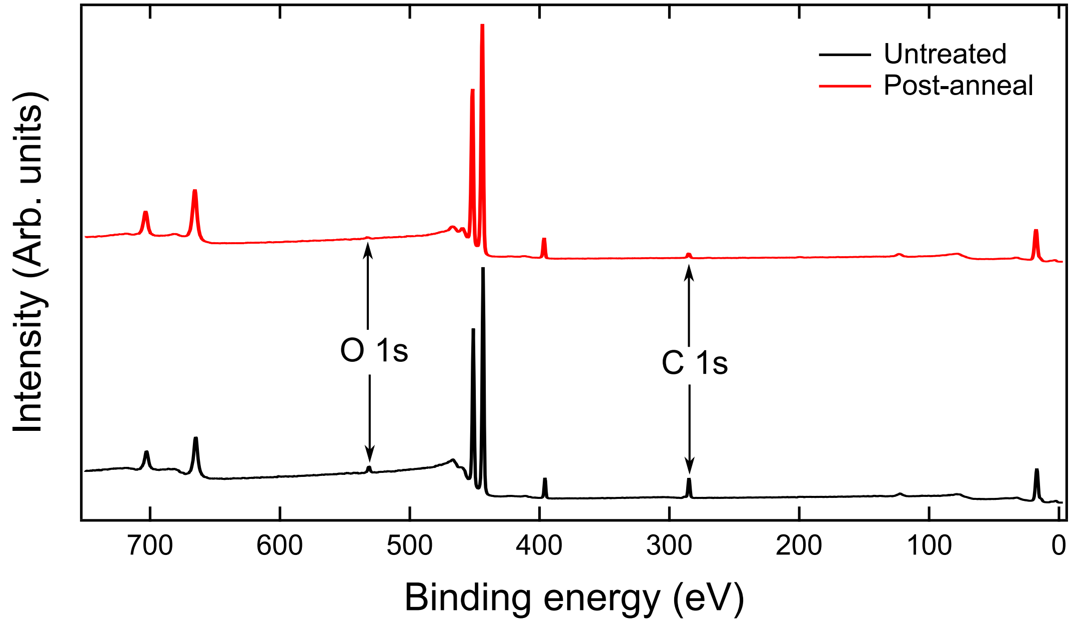

Figure 5.1: Offset survey spectra of the In-polar c-plane sample before (black) and after (red) surface preparation, showing a large reduction in the C 1s and O 1s peaks.

was observed at 119.3 eV from the *c*-plane surface, shown in Figure 5.3. It was also noted that the absence of a feature close to the Fermi edge in the valence band XPS spectra indicated an absence of metallic indium droplets at the surface, which may be caused by some surface cleaning treatments.

Following initial XPS measurements of core level peaks and determination of the separation of the VBM and surface Fermi level (ξ), the prepared sample was then exposed to sulfur from an electrochemical cell. A schematic of the cell design, first described by Wagner [95], is shown in Figure 5.4. The cell consists of a silver sheet, a AgI pellet, a Ag_2S pellet and a platinum mesh as the anode. The glass pistons are pressed into the cell using springs to ensure good electrical contact as the vaporisation of sulfur causes the volume of the cell to decrease. The cell is heated to 200 °C, to allow mobility of the Ag^+ ions within the Ag_2S pellet, before a potential is applied across the cell. In the Ag_2S pellet, both the Ag^+ ions and the electrons are mobile, maintaining a constant Ag/S ratio through the pellet. Silver may be added to, or removed from the Ag_2S pellet by passing a current across the cell. In the setup shown,

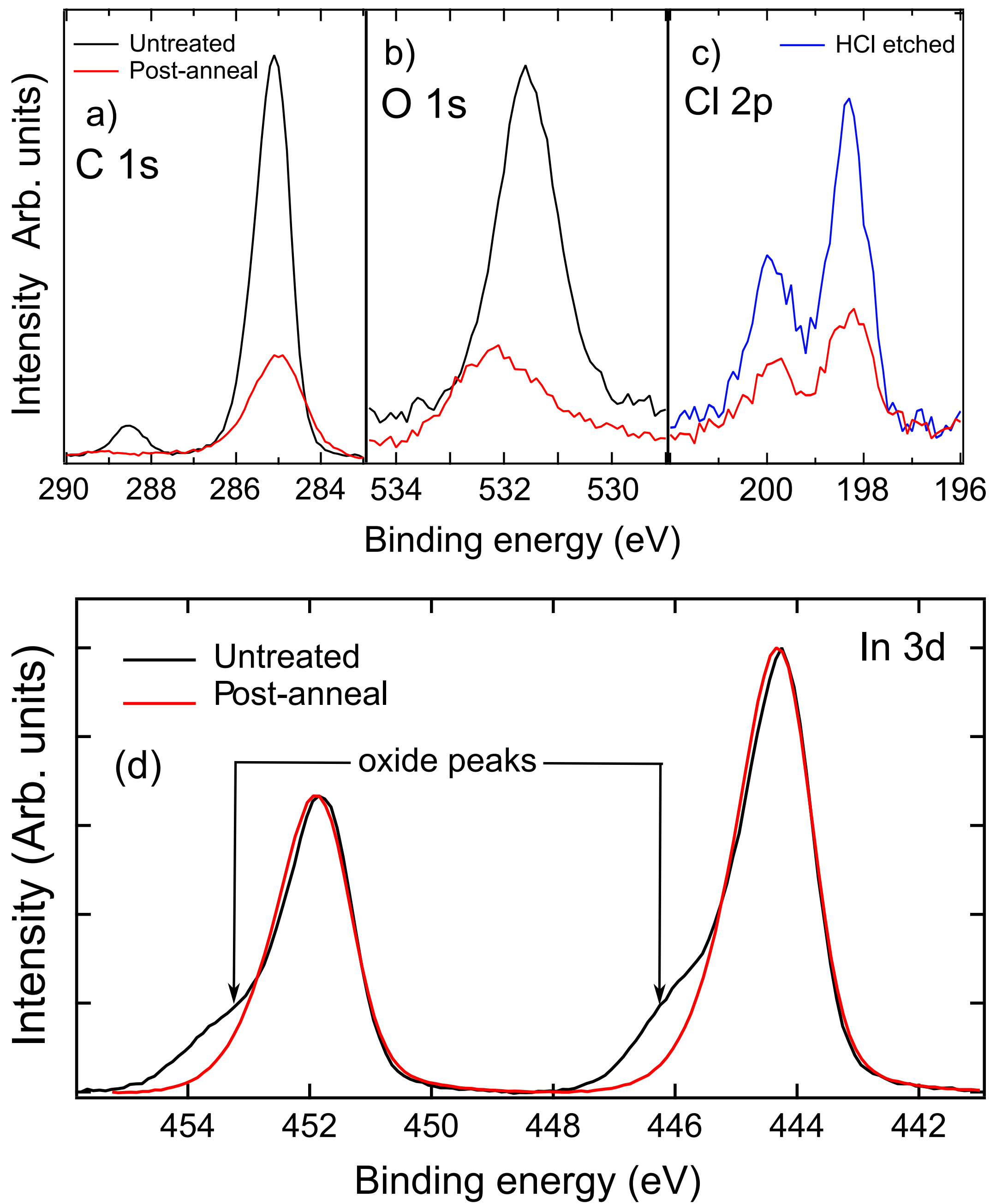

Figure 5.2: XPS data showing (a) the reduction of the O 1s, (b) C 1s and (c) Cl 2p peaks and (d) the removal of the oxide peaks at 446 eV and 453.5 eV in the In 3d region after the etch and annealing process. This process consisted of immersing the sample in 30 % HCl solution for 90 s followed by annealing the sample for 2 hours at 320 °C.

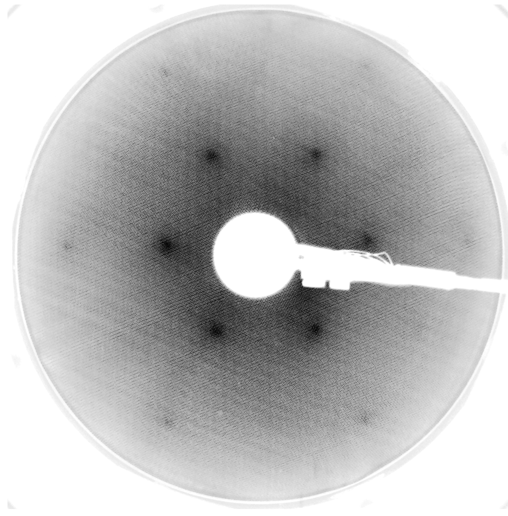

Figure 5.3: LEED image of the cleaned In-polar c-plane InN sample, showing a clear (1×1) pattern, recorded with an incident electron beam energy of 119.3 eV.

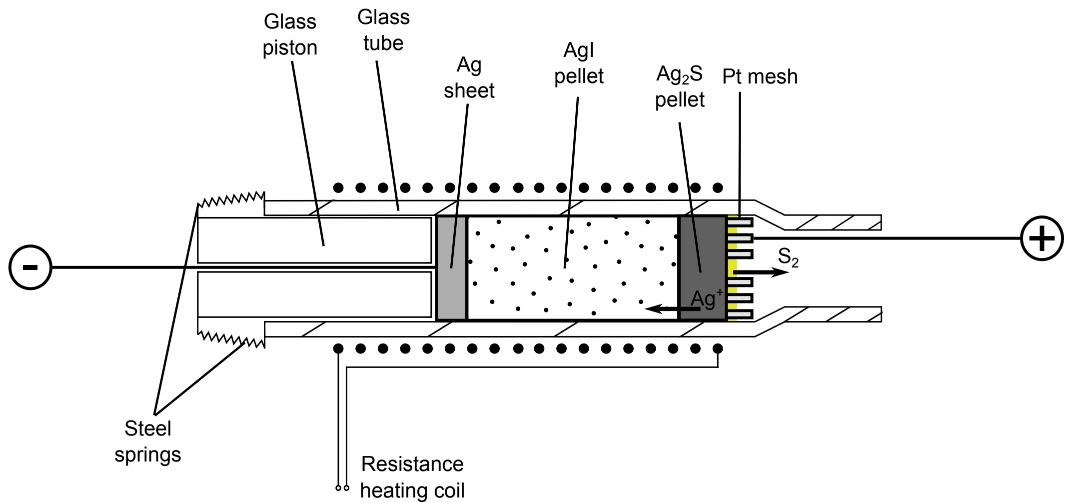

Figure 5.4: Schematic of the electrochemical cell used to deposit sulfur on the surface of the InN samples. With the cell heated to 200 °C, applying a potential across the cell allows Ag to be added to or removed from the Ag_2S pellet. When the Ag concentration decreases to a critical value, sulfur sublimes on the surface and vaporises into the vacuum chamber.

silver is removed from the pellet. Once the Ag/S ratio has decreased to a critical amount, liquid sulfur is formed as a new phase. Under UHV conditions and at 200 °C, the sulfur vaporises and fills the vacuum chamber, with the rate of sulfur arriving at the surface of the InN sample varying as a function of the pressure of the sulfur vapour. The sulfur vapour has been shown to be almost entirely composed of S_2 molecules [96].

5.3 Results and analysis

5.3.1 *a*-plane InN

The initial valence band XPS measurements from the cleaned sample showed a VBM to surface Fermi level separation of $\xi = 1.40 \pm 0.05$ eV and the Fermi level was found to lie 0.47 eV above the CBM using the calculations outlined in section 3.2. Sulfur was deposited on the sample using the electrochemical cell described above, with the sample at room temperature. XPS measurements were then taken between depositions of sulfur to show the evolution of the electronic structure of the surface as the total exposure increased. The measurements taken after 270 L of sulfur exposure show a slight charging effect thought to be due to the sample becoming slightly dislodged in the transfer process. This only affected one set of XPS measurements. In this case, the position of the Fermi level is calibrated using the C 1s peak positions relative to those of the measurements for the clean sample and for the sample at the preceding and succeeding exposure times. The binding energy scale was shifted by the average difference in binding energy with these C 1s peaks, and the larger error bars reflect the range of values of these peaks. The valence band spectra indicated a gradual decrease in ξ, of up to 0.26 ± 0.05 eV for the greatest exposure, shown in Figure 5.5. The rate of decrease of ξ appears to slow after ~600 L, implying that a minimum ξ has been reached. This could be due to a saturation of sulfur on the surface, such that further bonding of sulfur to indium is prevented, or that most of the unoccupied donor-like states at the surface have been occupied.

By applying the space charge calculations outlined in chapter 3, a gradual reduction in band bending from 0.28 eV to 0.02 eV is observed over the

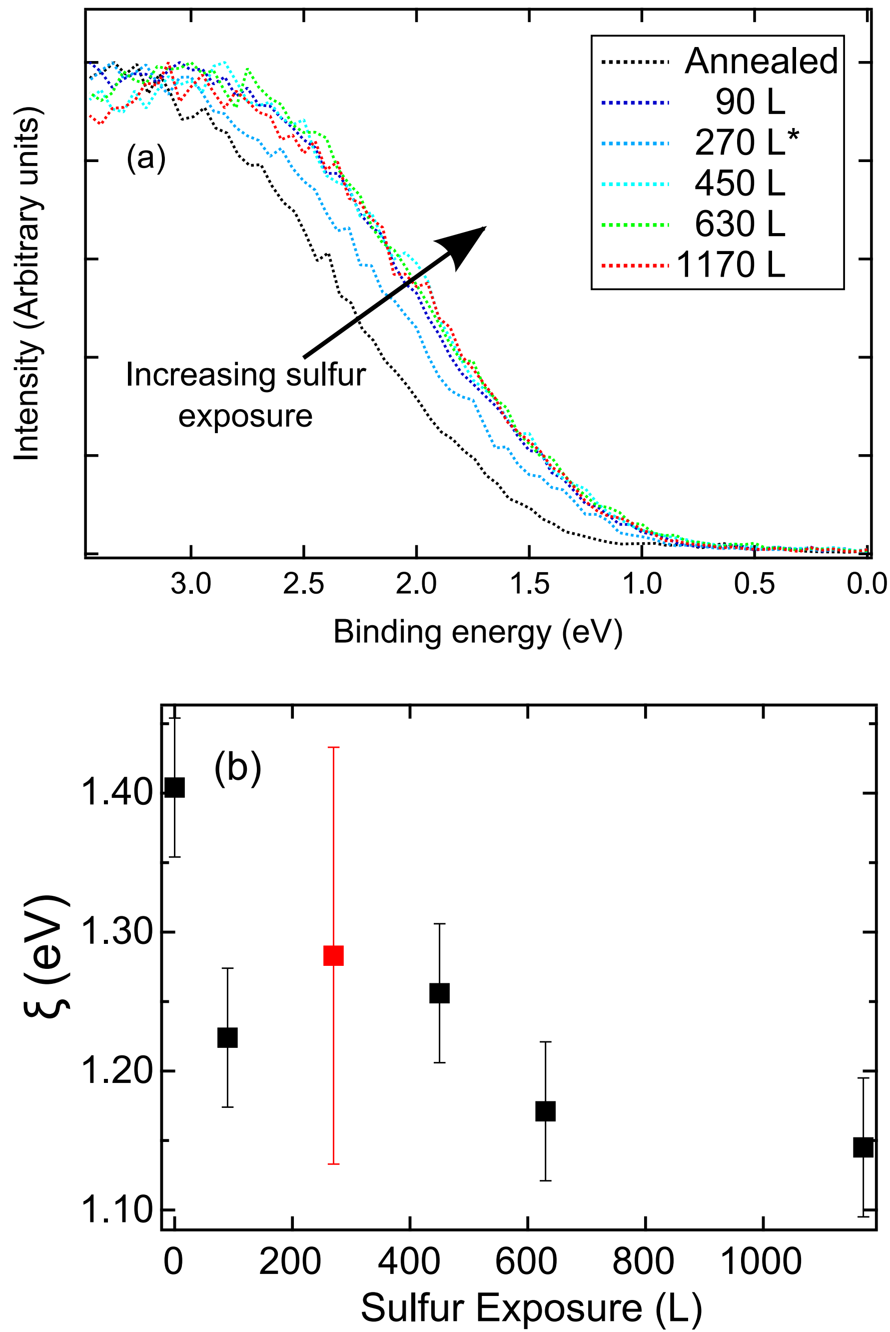

Figure 5.5: a-plane sample (a) valence band spectra during the sulfur deposition process and (b) ξ plotted against sulfur exposure, showing a decrease in ξ with sulfur exposure. Starred ($*$) and red data indicates sample charging, where binding energy was referenced from the C 1s peak.

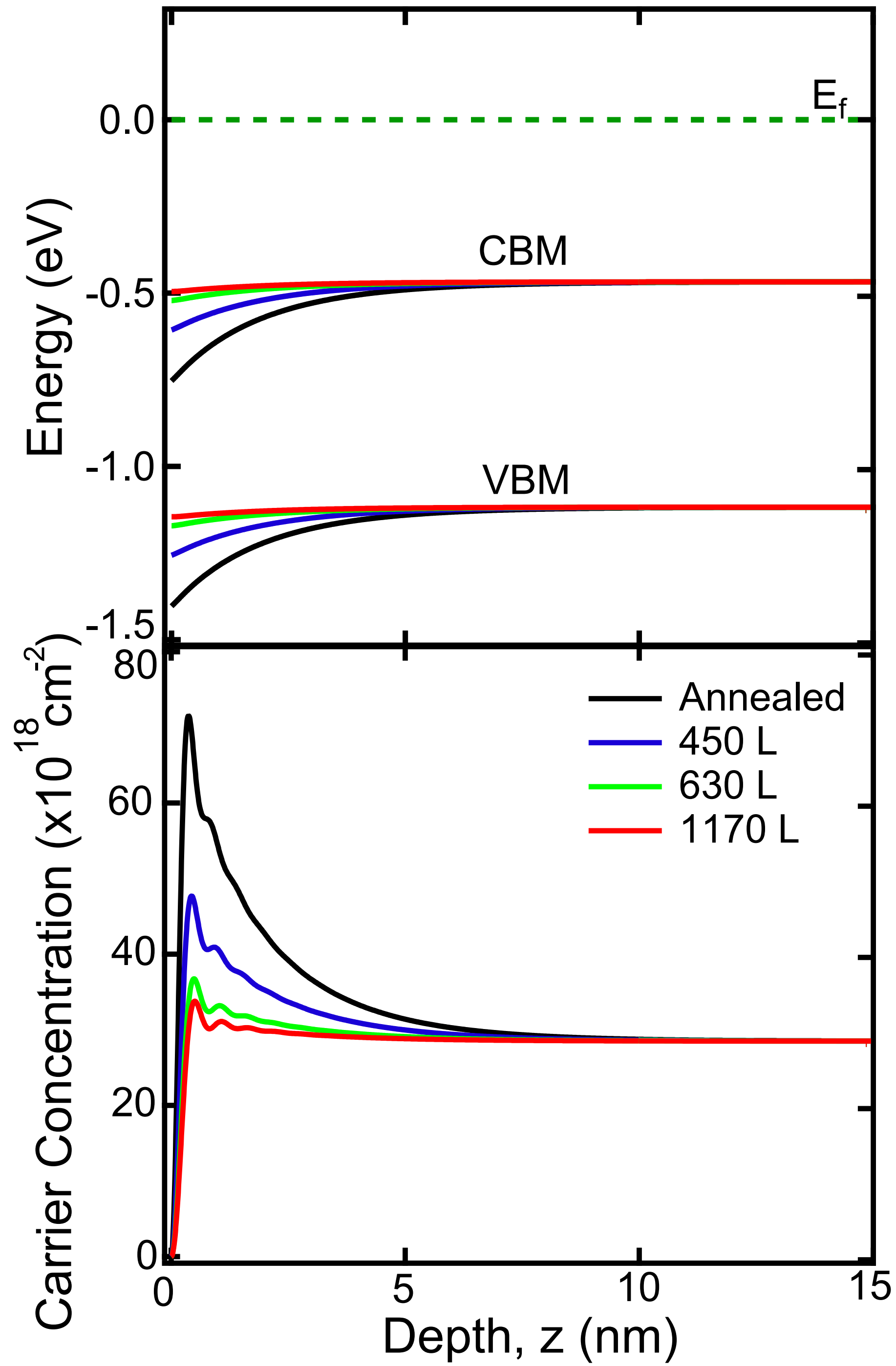

Figure 5.6: Numerically calculated band bending and charge carrier concentration profiles for the a-plane InN sample at various stages of sulfur deposition, showing a trend towards flat bands as the sample is exposed to more sulfur. These profiles were carried out using the calculations detailed in chapter 3.

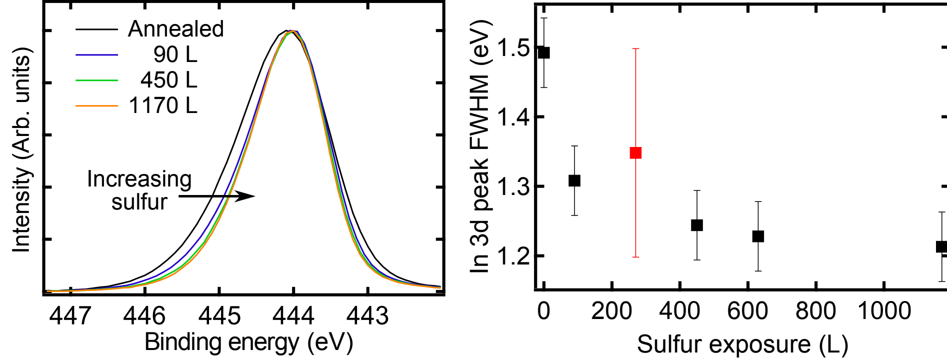

Figure 5.7: Decrease in FWHM of the In $3d_{5/2}$ peaks as sulfur exposure is increased for the a-plane sample. This is interpreted as a reduction in plasmon losses caused by the electron accumulation layer. Red data marker indicates sample charging. The binding energy of the In 3d peaks was aligned for comparison.

duration of sulfur exposure, and these are shown in Figure 5.6. The near-flat bands observed after 1170 L exposure implies that a complete removal of the electron accumulation layer has been achieved for this sample. As the sample appears to exhibit no electron accumulation layer at the highest exposure to sulfur it is inferred that the reason for the decreased rate of reduction of ξ observed in Figure 5.5(b) is due to the occupation of most of the donor-like states.

Supporting evidence for the significant reduction in the electron accumulation can be observed in changes in the In 3d peaks. If the surface electron accumulation is decreasing, it would be expected that the full-width at half-maximum (FWHM) of the asymmetric peaks would decrease due to a reduction in conduction band plasmon losses [73]. For the electron densities considered, the plasmon energy is of the order of 250-400 meV [49, 73]. This decrease is indeed observed during deposition of sulfur on InN, despite the broadening which would be expected due to the chemical shift of In–S bonds. The In $3d_{5/2}$ peaks and FWHMs are shown in Figure 5.7 and Table 5.1, and show a reduction from 1.49±0.05 eV on the untreated sample to 1.25±0.05 eV after 1170 L of sulfur exposure.

Looking at the S 2p region of the XPS spectra after 90 L exposure to sulfur (Figure 5.8(a)), fully constrained doublet peaks are fitted to the spectra using the method described in section 2.1.1, with the binding energy

of the peaks indicative of In–S–S–In bonds at 161.8 eV [88]. There is also a component due to elemental sulfur observed at 163.5 eV. No bonding of sulfur to oxygen was observed. After the final deposition of sulfur on the surface, another bonding environment due to In–S–In bonding was observed at 161.2 eV, as shown in Figure 5.8(b).

With the data gathered at intervals throughout the sulfur deposition process, it is possible to show the development of each of the peaks representing the bonding environments as a function of exposure to sulfur. This is done by normalising the S 2p region spectra to the background level to account for (slight) variations in x-ray flux between scans. The peak area of each of the doublet peaks can then be plotted against sulfur exposure, as shown in Figure 5.9(a). The percentage of each bonding environment within the S 2p region can also be plotted in this way (Figure 5.9(b)).

Considering Figure 5.9 and Table 5.1, one can clearly see that initially the In–S–S–In bonding environment is preferred. The S–S bonds then break as more sulfur is deposited, and the In–S–In bonds become more favourable. However, both bonding environments contribute to the reduction of unoccupied donor-like states at the surface resulting in a lowering of the electron accumulation. After this point, the trend slowly reverses as ξ stabilises. The amount of elemental sulfur on the surface slowly increases throughout the deposition of sulfur. Its effect is unknown, however, it may be drawing electrons away from the accumulation layer due to its high electronegativity relative to In (Pauling scale 2.58 vs. 1.78 for In [62]).

*Table 5.1: Summary of changes in ξ, In 3d FWHM and sulfur bonding environments with the deposition of sulfur onto the a-plane InN sample, showing a decrease in plasmon losses associated with surface electron accumulation. * Indicates slight sample charging (binding energy referenced to C 1s peak).*

Exposure (L)	ξ ±0.05 (eV)	In 3d FWHM ±0.05 (eV)	In–S–In %	In–S–S–In %
0	1.40	1.49	—	—
90	1.22	1.31	0	88
270*	1.28	1.35	0	75
450	1.26	1.24	40	33
630	1.17	1.23	38	29
1170	1.14	1.21	27	35

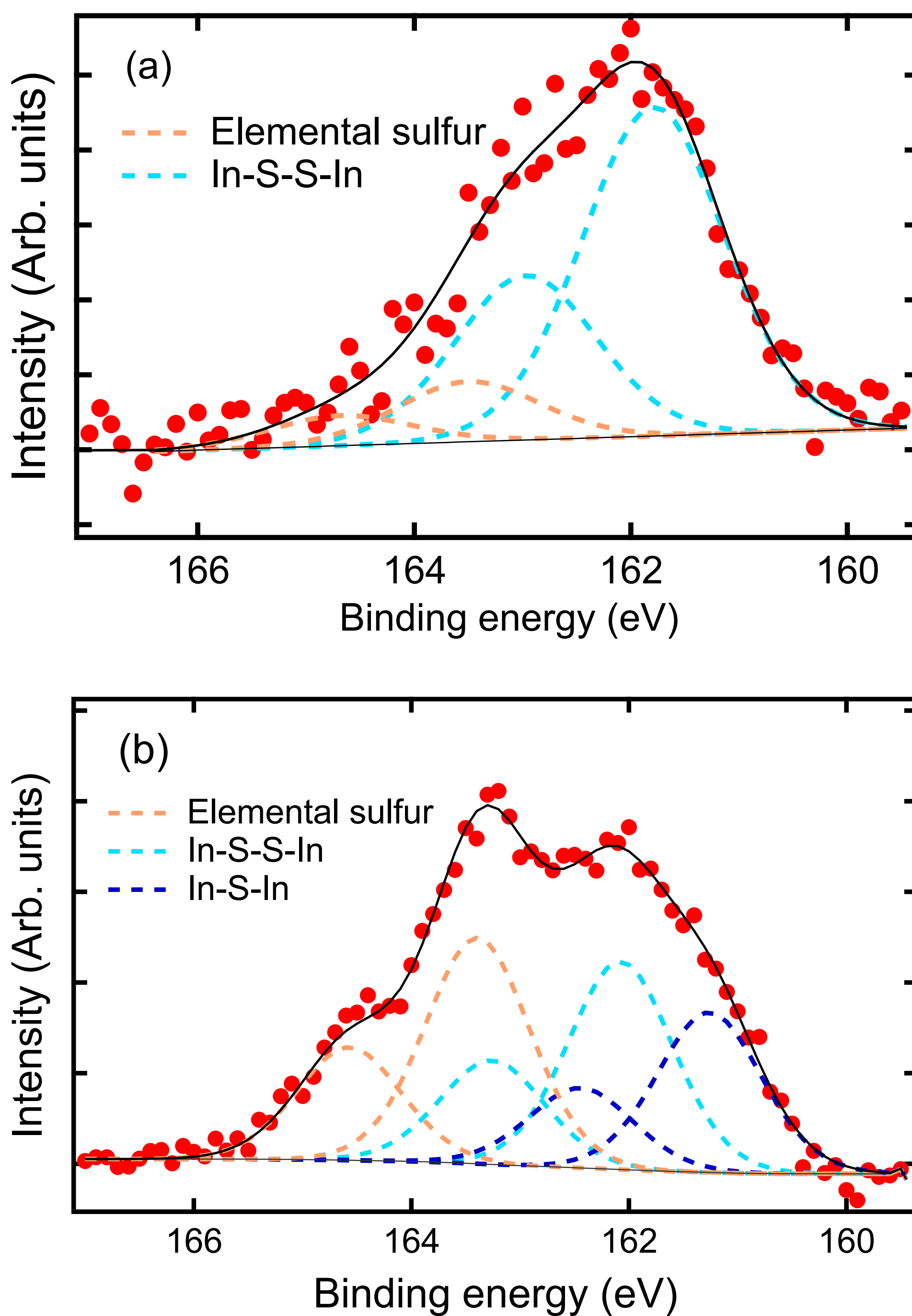

Figure 5.8: S 2p region of the XPS spectrum after (a) 90 L and (b) 1170 L of sulfur exposure to the InN a-plane sample. Doublet peaks were fitted at previously observed [66–68] values corresponding to In–S–In bonding (~161.0 eV), In–S–S–In bonding (~162.0 eV) and elemental sulfur (~163.5 eV).

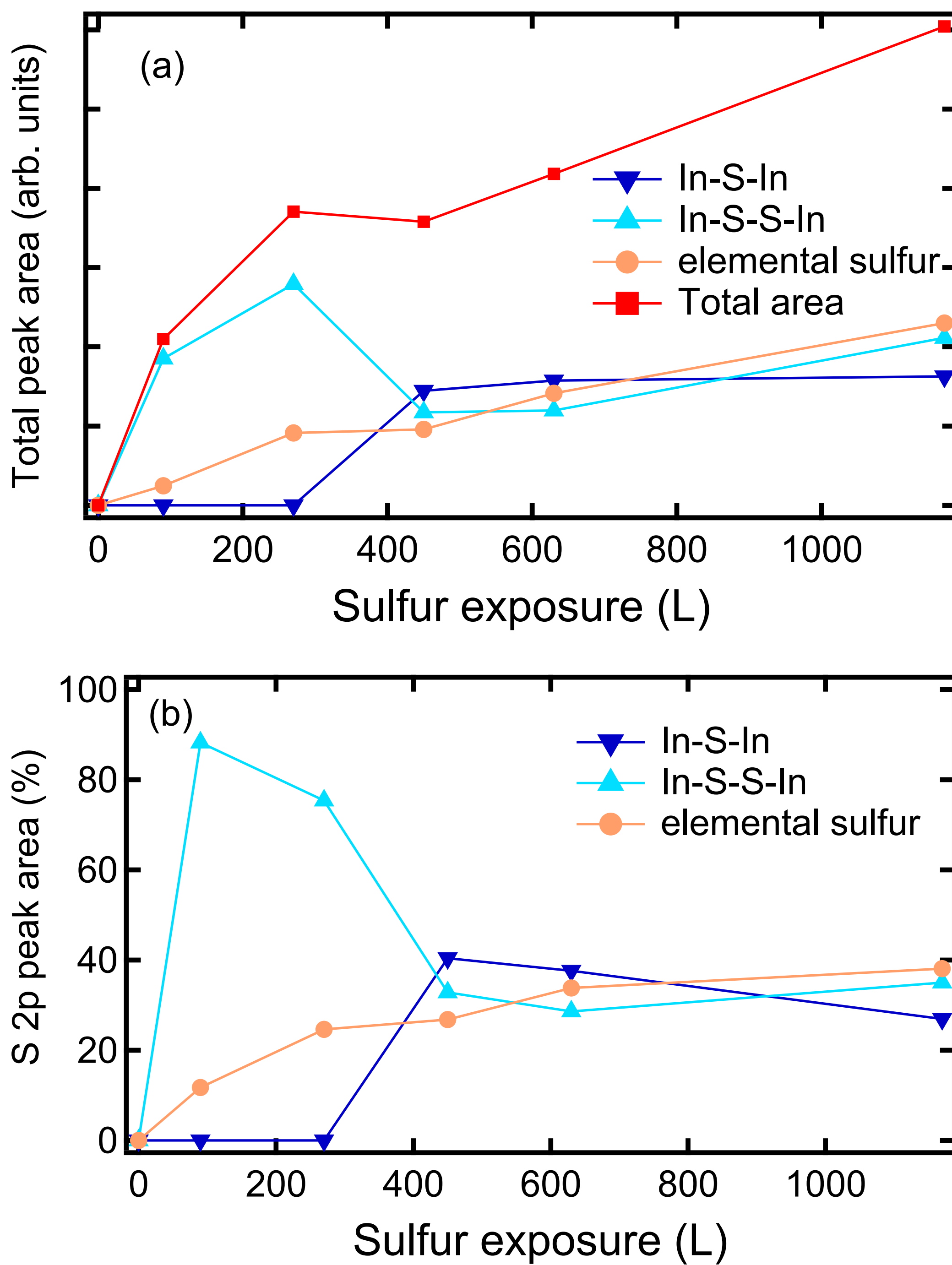

Figure 5.9: Development of the areas of (a) the different bonding environment components and (b) as a percentage of the total S 2p peak area as sulfur exposure is increased. Initially, only In–S–S–In bonding is observed, with this being partially replaced by In–S–In bonding after 450 L. The amount of elemental sulfur at the surface increases steadily throughout the sulfur exposure.

5.3.2 In-polar *c*-plane InN

For the In-polar c-plane sample a similar procedure was carried out as detailed above for the a-plane sample. Initial valence band spectra indicated that ξ was 1.42 eV prior to sulfur deposition and the Fermi level was found to lie 0.11 eV above the CBM, indicating a band bending of 0.66 eV. This band bending was much greater than for the a-plane sample, due to non-intrinsic nature of the In-adlayers on the a-plane surface [53, 97], and led to a significantly larger (relative to the bulk) electron accumulation layer. Sulfur deposition took place with the sample held at 200 °C in an effort to increase uptake and mobility of sulfur on the surface [93]. XPS measurements were also taken at more frequent intervals throughout the sulfur deposition to provide more insight into the interplay between various bonding configurations on the surface.

Figure 5.10(a) shows the valence band region of the sample as a function of sulfur exposure, illustrating the decrease in ξ (Figure 5.10(b)). These data have been fitted with an exponential and a double exponential lineshape of the forms

$$\xi = A_0 + A_1 \exp\left[-\frac{x}{\gamma_1}\right] \tag{5.1a}$$

and

$$\xi = B_0 + B_1 \exp\left[-\frac{x}{\tau_1}\right] + B_2 \exp\left[-\frac{x}{\tau_2}\right] \tag{5.1b}$$

respectively, where x is the exposure to sulfur, and A_i and B_i are energy constants and γ and τ_i are exposure constants for process i. Exponential equations were chosen for the fit because the rate of reduction in ξ diminishes as sulfur exposure increases. The two fits give χ^2 values of 0.0036 and 0.0021 respectively, indicating that the difference between them is not statistically significant when considering the additional degrees of freedom in the double exponential fit. However, in this chapter the double exponential fit will be proposed as a plausible model in light of additional information presented. The presence of two exposure constants in the double exponential fit would imply the presence of two processes involved in the decreasing of ξ through the addition of more sulfur to the InN surface, which will be looked at more closely later in order to justify this choice of lineshape. The total decrease in ξ was found to be 0.23±0.05 eV, effectively the same as for the a-plane sample.

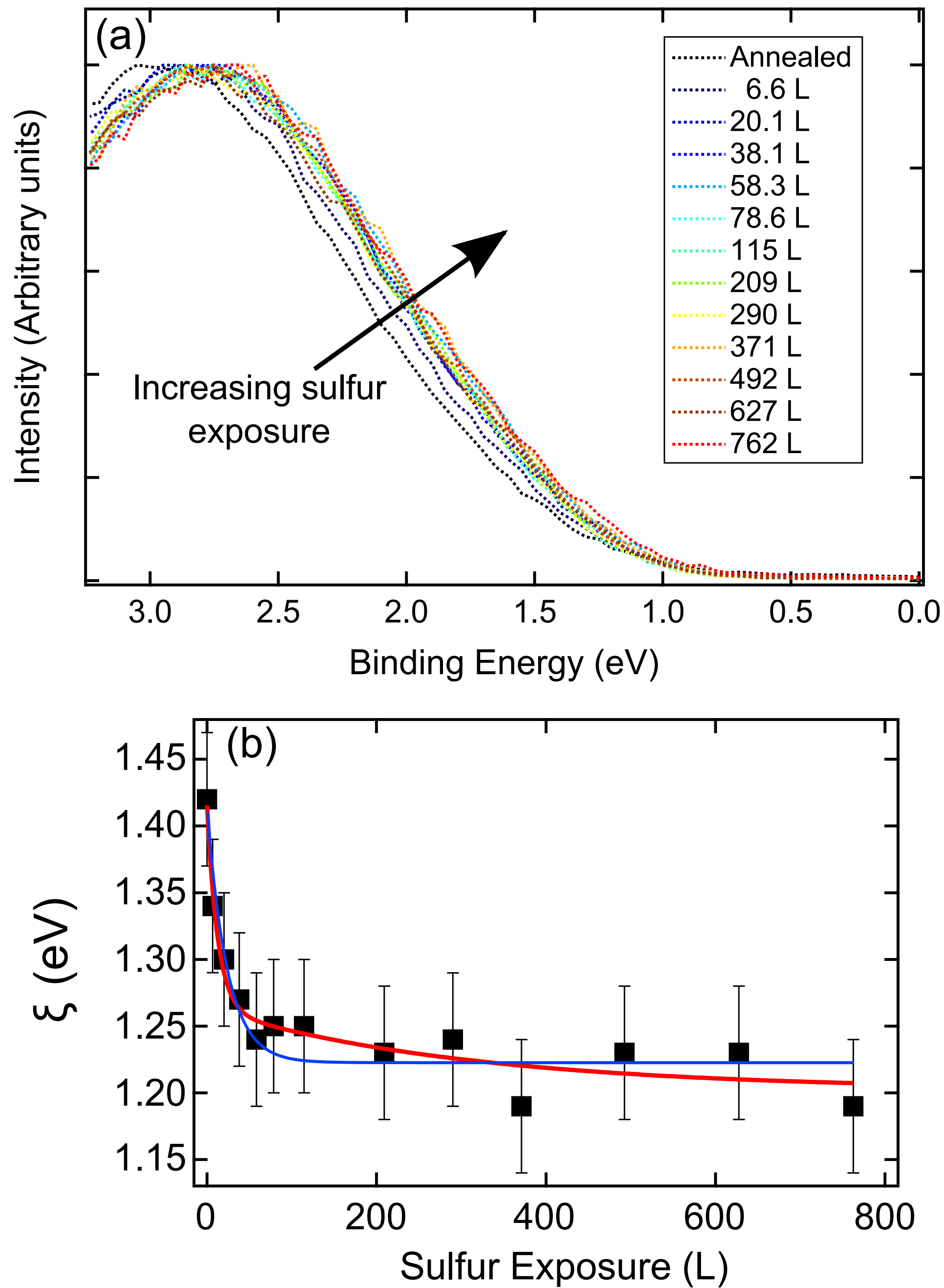

Figure 5.10: (a) Normalised valence band spectra for the In-polar c-plane sample during the sulfur deposition, showing a decrease in binding energy for the leading edge as sulfur exposure increased, and (b) the separation of the VBM and the Fermi level plotted with respect to sulfur exposure. This has been fitted with a single (blue) and a double (red) exponential, given in Equation 5.1.

Through the theoretical methods detailed in chapter 3, band bending and charge carrier concentration as a function of depth were calculated for the sample at intervals throughout the sulfur deposition process. These calculations reveal a reduction in surface electron sheet density from 4.61×10^{-13}cm^{-2} to 2.21×10^{-13}cm^{-2}, a reduction in the electron accumulation of ~55 % – much larger than any previous attempts at reduction on polar n-type InN, and are shown in Figure 5.11(a). Although the total reduction in band bending was the same as for the *a*-plane sample, the position of the Fermi level above the CBM in the bulk is much higher for the *c*-plane sample, therefore the initial band bending was much greater (0.66 eV as opposed to 0.28 eV). A narrowing of the In 3d peaks was also observed as a consequence of the reduction in conduction band plasmons, which is shown in Figure 5.12 and Table 5.2. A greater comparison between the two surfaces studied will be explored in subsection 5.3.3.

Inspecting the S 2p region after a sulfur exposure of just 6.6 L, Figure 5.13(a) reveals that the main bonding environment present is In–S–In, with a small amount of In–S–S–In bonding also present. However, after the final deposition of sulfur, In–S–S–In bonding is the dominant environment, with elemental sulfur also present (Figure 5.13(b) and Table 5.2). A steady increase in amorphous elemental sulfur is proposed as the reason for a decrease in spot intensity from LEED images (not shown) taken throughout the deposition process.

Analysing the S 2p peak areas in the same way as for the *a*-plane sample, it becomes evident that the interaction of sulfur with the In-polar *c*-plane sample is very different (Figure 5.14(a)). The initial bonding is largely In–S–In, however, the proportion of this environment decreases after 6.6 L and is replaced as the dominant component by In–S–S–In bonding. After an initial rapid change in dominant bonding environment, the ratio of the peaks corresponding to In–S–S–In bonded sulfur to In–S–In bonded sulfur settles at approximately 5.7 : 1 as the number of indium atoms on the surface available for sulfur atoms to bond to reduces. Elemental sulfur on the surface was also observed to increase slowly as the total sulfur exposure increased. This information can then be used in conjunction with the data from the valence band region to gain an overall picture of the processes at work.

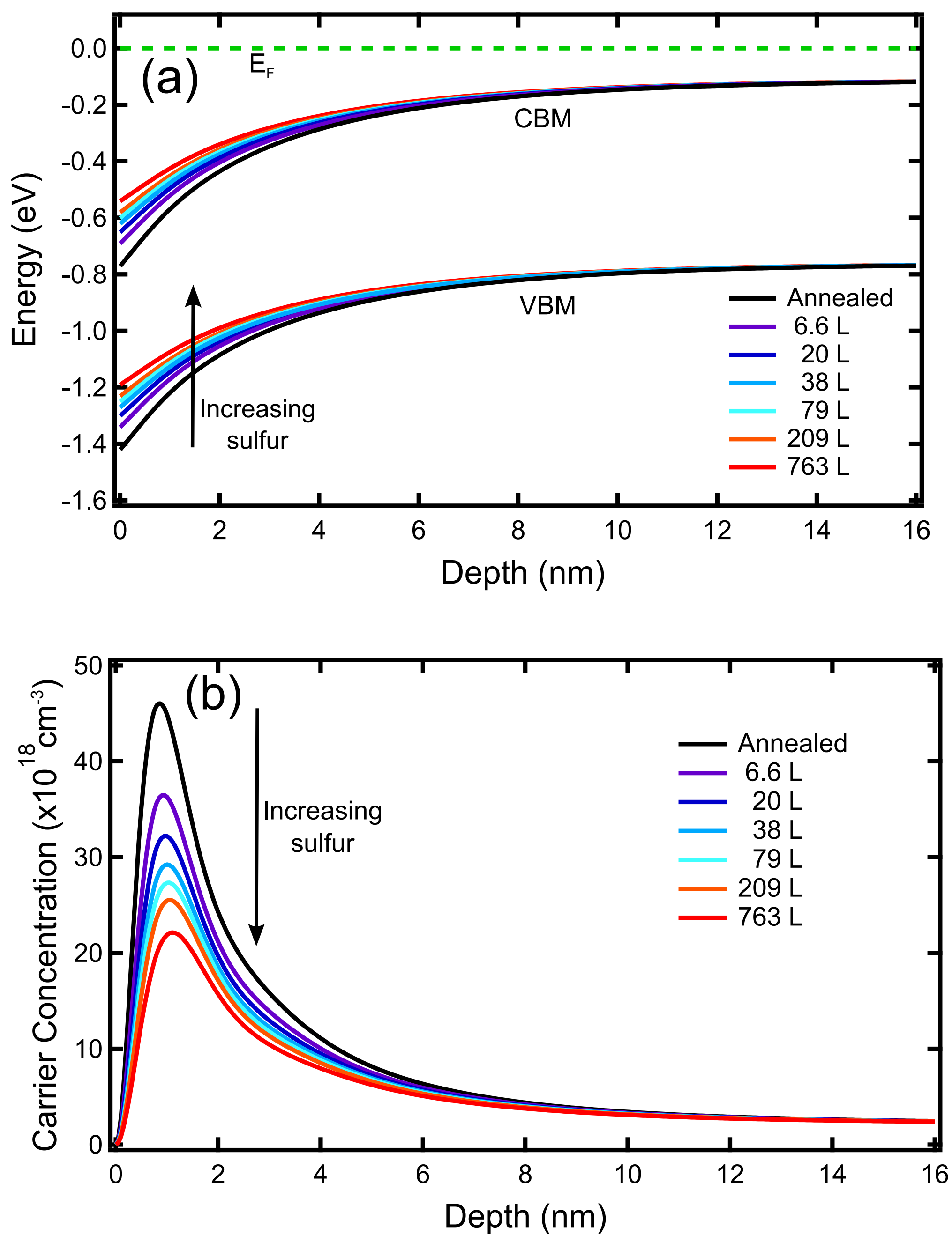

Figure 5.11: Numerically calculated (a) band bending and (b) charge carrier concentration profiles at the surface of the In-polar c-plane InN sample at various stages during sulfur deposition. A decrease in band bending and charge carrier concentration at the surface is observed as sulfur exposure is increased.

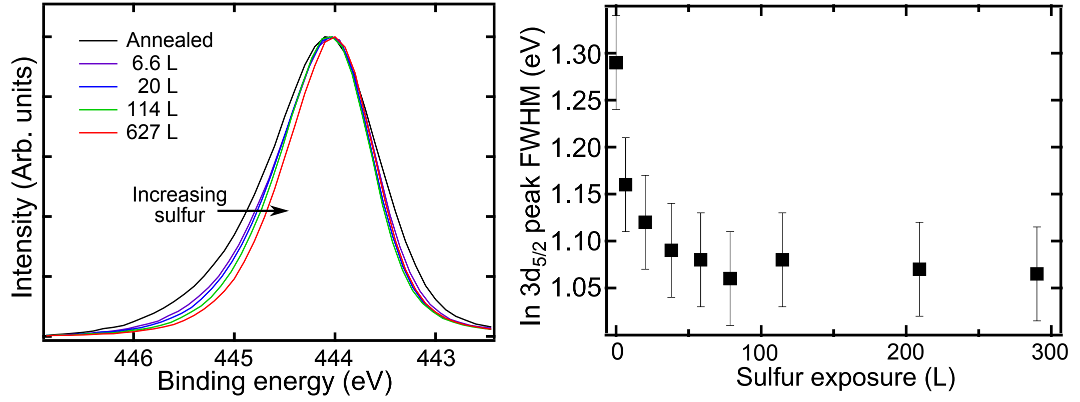

Figure 5.12: Reduction in the tail on the high-binding energy side of the In $3d_{5/2}$ peak is attributed to a decrease in plasmon losses caused by electrons in the electron accumulation layer. A selection of points are shown for clarity.

Table 5.2: Summary of changes in ξ, In 3d FWHM and sulfur bonding environments with the deposition of sulfur onto the In-polar c-plane InN sample.

Exposure (L)	ξ ±0.05 (eV)	In 3d FWHM ±0.05 (eV)	In–S–In %	In–S–S–In %
0	1.42	1.29	—	—
6.6	1.34	1.16	67	33
20	1.3	1.12	40	47
38	1.27	1.09	30	55
58	1.24	1.08	25	61
79	1.25	1.06	17	67
115	1.25	1.08	19	64
209	1.23	1.07	17	65
290	1.24	1.07	15	67
371	1.19	1.07	12	69
493	1.23	1.07	12	68
628	1.23	1.06	13	68
763	1.19	1.08	13	69

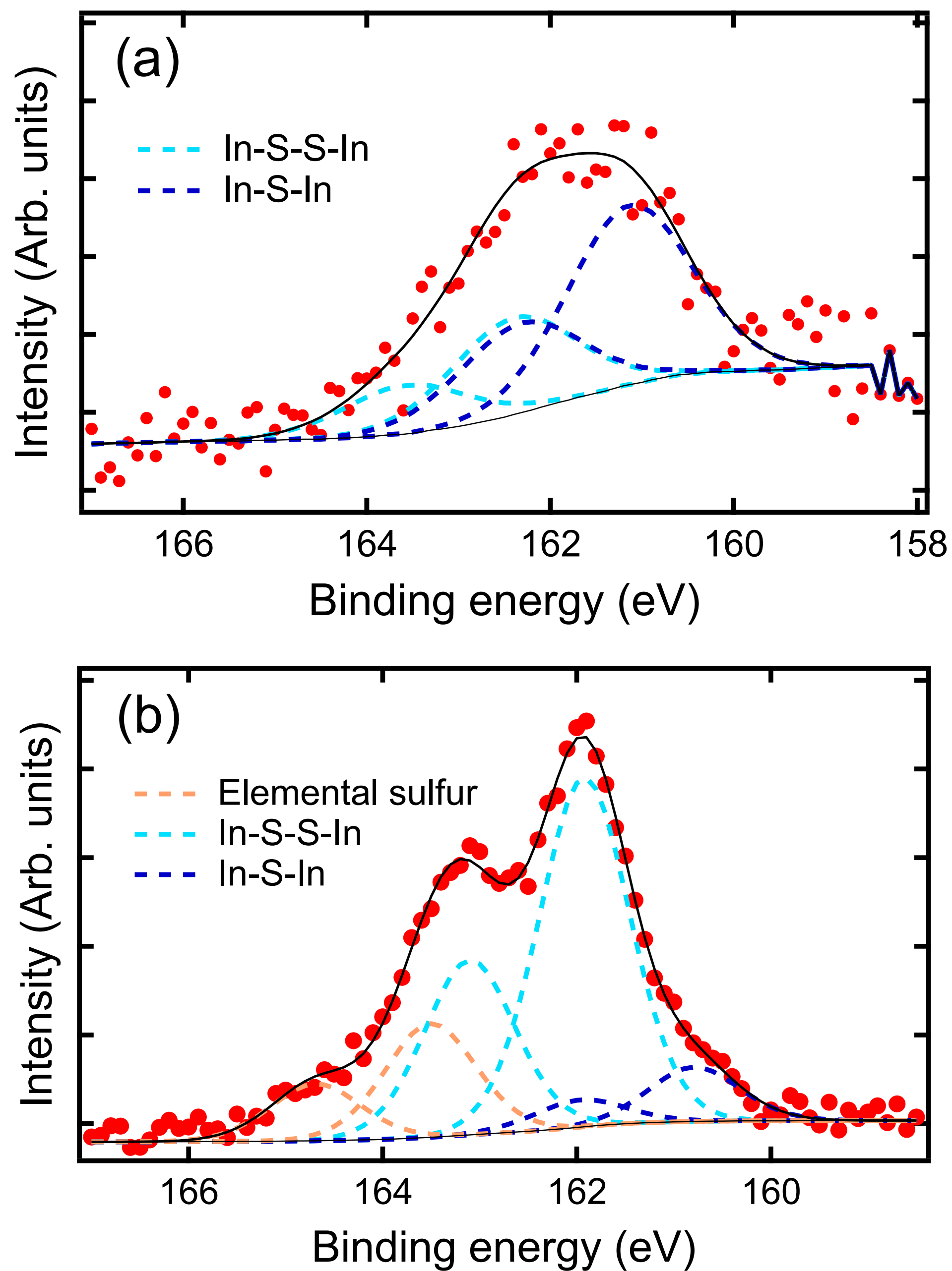

Figure 5.13: S 2p region of the XPS spectrum after the (a) 6.6 L and (b) 763 L in-situ exposure of sulfur to the c-plane InN sample. As for the a-plane sample, doublet peaks were fitted at previously observed [66–68] values corresponding to In–S–In bonding (~161.0 eV), In–S–S–In bonding (~162.0 eV) and elemental sulfur (~163.5 eV).

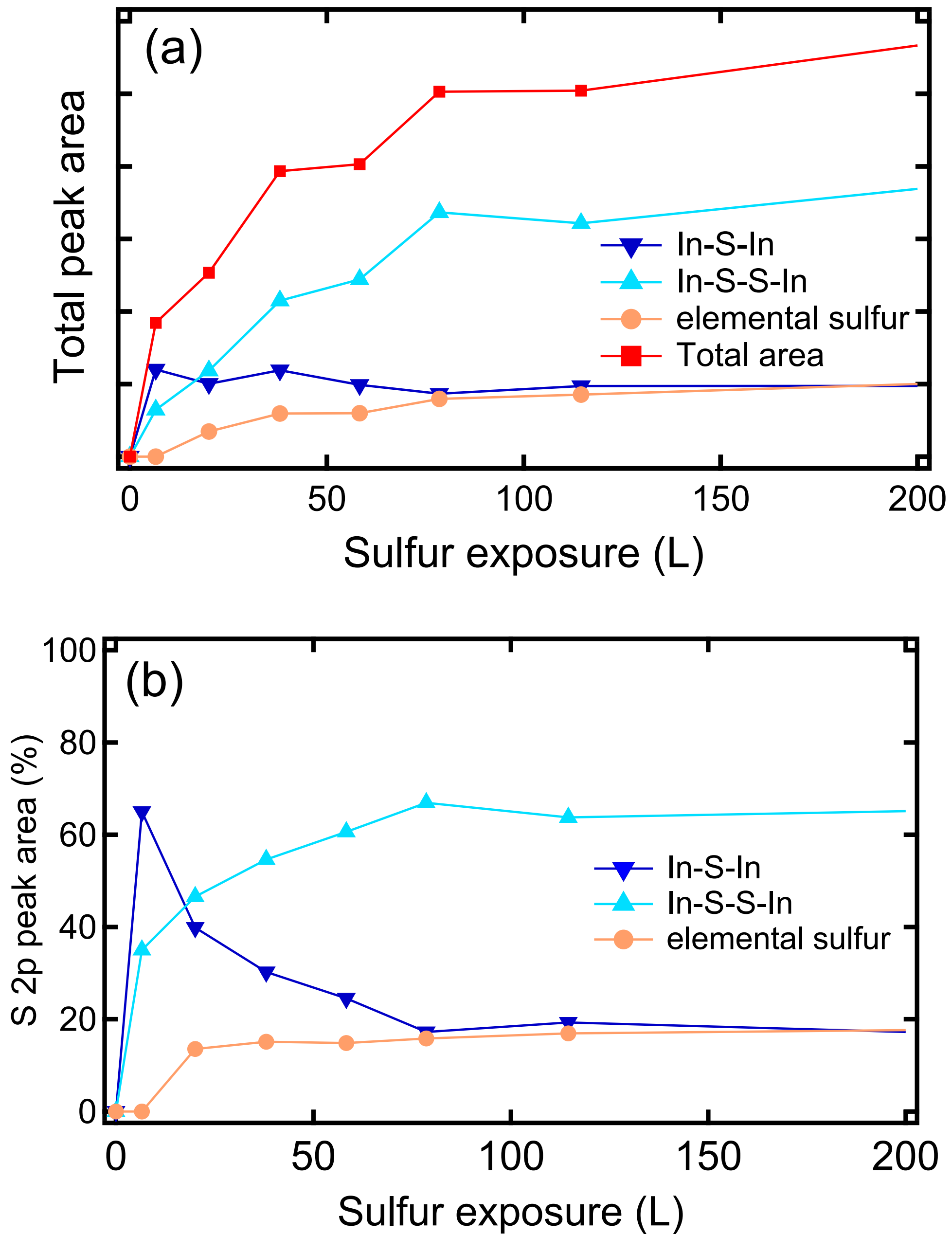

Figure 5.14: Initial development of the areas of (a) the different bonding environments and (b) as a percentage of the total S 2p peak area as sulfur exposure is increased. This development is clearly different to observations of the a-plane sample, with In–S–In bonding being the dominant configuration at low sulfur exposure. However, this is largely replaced by In–S–S–In bonding after ~20 L of exposure. Elemental sulfur is again seen to steadily increase with sulfur exposure.

In Figure 5.10(b), a double exponential of the form shown in Equation 5.1 was used to fit the decrease in ξ as sulfur exposure increased. The values assigned to the constants during the fitting procedure are as follows:

- $\tau_1 = 12.4$ L
- $\tau_2 = 305$ L
- $B_0 = 1.20$ eV
- $B_1 = 0.152$ eV
- $B_2 = 0.061$ eV.

One exposure constant, τ_1, can easily be assigned to the decrease in surface area of the sample where a sulfur atom may arrive to form a bond with two indium atoms due to the rapid onset and subsequent decrease in Figure 5.14(a). It is proposed that the process related to the second exposure constant, τ_2, is due to the formation of the In–S–S–In bonds through the addition of an extra sulfur atom to an In–S–In environment, though understanding the precise structural details of this process requires additional density functional theory (DFT) and scanning tunnelling microscopy (STM) studies. Such an approach will:

- resolve where the sulfur atoms sit on the surface;
- determine the point at which In–S–S–In bonding becomes more energetically favourable due to a lack of indium atoms available;
- determine the sticking factor for sulfur atoms joining the In–S–In environment.

The energy constants B_1 and B_2 indicate the total decrease in ξ due to their respective processes, such that τ_i is the total sulfur exposure required for process i to reduce ξ by an amount $(B_i - B_i/e)$. From the values of τ_i and B_i it can be seen that the formation of In–S–S–In bonds at the surface results in a greater decrease in ξ than the initial In–S–In environment, though this process requires a higher coverage of sulfur atoms.

The other energy constant, B_0, is a minimum for the value of ξ achievable for this sample and corresponds to a reduction in band bending of 0.24 eV. It is thought that this value is related to various factors, such as the number of adsorbates on the surface (as the sample was not completely free of contamination), how well ordered the sample is, and the smoothness of the sample

(as roughness increases the surface area of the sample and thus the places where sulfur can bond to indium atoms). However, from these experiments it is not possible to determine an accurate theoretical minimum achievable value for B_0.

5.3.3 Comparison of *a*-plane and In-polar *c*-plane InN

By comparing the results for the *a*-plane sample with those for the In-polar *c*-plane sample, the total decrease in ξ is effectively the same in both cases. This is despite the fact that the interaction of sulfur at both surfaces is clearly very different when comparing preferential bonding configurations (see Figures 5.9 and 5.14). On the In-polar *c*-plane, In–S–In bonds are formed initially, and are replaced by In–S–S–In bonds, however, the inverse happens on the *a*-plane sample. This is due to differing interatomic spacings and arrangements between indium atoms at the different surfaces. The surface reconstruction of In-polar *c*-plane samples has primarily been investigated through photoemission and co-axial impact collision ion scattering spectroscopy (CAICISS), however, little is known about the termination of the *a*-plane surface, except the presence of ~3 monolayers of indium adlayers [52]. A comparison of the peak positions shows that S–In interlayer separation or sulfur adsorption sites on the *a*-plane surface are different from those on the In-polar *c*-plane surface, with the binding energy of the In–S–In component is slightly lower for the *c*-plane sample (160.9±0.1 eV instead of 161.3±0.1 eV). This is due to the proximity of valence electrons to the each sulfur atom which are able to more efficiently screen the core hole left by a photoelectron, thus reducing its binding energy. As the binding energy of the In–S–In component for the *c*-plane sample is shifted as such, it can be inferred that the sulfur atoms in this environment have a greater overall proximity to the In adlayers. However, a complete picture of differing sulfur adsorption sites on these surfaces requires a structural investigation using techniques such as DFT, CAICISS, medium energy ion scattering (MEIS) and LEED intensity-voltage curve analysis.

From the values obtained for the constants in Equation 5.1, it is inferred that In–S–S–In bonding produces the largest reduction in ξ. If this can be extended to the *a*-plane sample, then it would imply that as In–S–S–In bonding

is replaced by In–S–In bonding, this would slightly reduce the reduction in ξ. Looking again at Figure 5.5(b) (and ignoring the possibly erroneous data point from sample charging), after 450 L of sulfur exposure, ξ is greater than at 90 L exposure. This coincides with the point in Figure 5.9 where In–S–S–In is replaced by In–S–In bonding, supporting the idea that In–S–S–In bonding produces a larger reduction in ξ and band bending than the formation of In–S–In bonding.

5.4 Conclusions

In this investigation, a series of sulfur depositions were carried out on HCl-etched *a*-plane and In-polar *c*-plane InN surfaces using an electrochemical cell to perform controlled sulfur exposure. In both cases, the valence band XPS showed that the separation of the VBM and Fermi level, ξ, decreases by ~0.25 eV due to sulfur forming In–S–In and In–S–S–In bonds at the surface. For the *a*-plane sample, where the bulk Fermi level lay much higher above the CBM due to its higher electron concentration, this eliminated the band bending observed on the post-etching sample. On the In-polar *c*-plane sample a 55 % reduction in electron accumulation was observed but flat bands were not achieved.

On the *a*-plane sample, In–S–S–In bonding dominated before being replaced with In–S–In bonding, whereas on the In-polar *c*-plane sample the inverse was observed. The binding energy of the In–S–In component for the *a*-plane sample was also higher than for the In-polar *c*-plane sample, providing evidence of differing adsorption sites between the two surfaces investigated. It was also discovered that In–S–S–In bonding had a greater effect in reducing ξ than In–S–In bonding on the *c*-plane sample, and from initial analysis this appears to also be the case for the *a*-plane sample. This method of sulfur deposition has therefore produced a greater reduction in ξ than previous chemical/ex-situ treatments, while also demonstrating the optimum bonding environments for the sulfur atoms. Further work on structure using LEED intensity-voltage curves, CAICISS, STM and DFT is required to truly understand structural effects.

Chapter 6

Summary and Conclusions

This thesis has investigated the modification and control of the electronic properties of the a-plane and In-polar c-plane surfaces of n-type InN. The surfaces of InN exhibit a strong downward band bending due to an extremely low CBM at the Γ-point, leading to the formation of an electron accumulation layer that is prohibitive for several device applications [20–22]. This electron accumulation layer is a feature of both n- and p-type InN and has been the subject of several studies. It has been observed that In adlayers form at the surface post-growth due to defects, creating donor-like defects which cause the observed strong band bending [25]. While the absence of adlayers and electron accumulation for a-plane InN has been observed directly after growth [97], to date only an in-situ cleaving of the a-plane surface has been shown to remove the In adlayers and associated electron accumulation layer once they have formed [54], as DFT studies have predicted that the adlayers are not intrinsic to this surface [53]. Other techniques attempted for the reduction of this electron accumulation layer have focussed on the deposition of the highly electronegative sulfur on the surface via the ex-situ technique of immersion in $(NH_4)_2S_x$ solution [66–68]. These surface treatments have met with moderate success, with sulfur bonds with indium reducing the number of unoccupied donor-like states in the In adlayers and reducing band bending by 0.15 eV, corresponding to a 30 % (70 %) decrease in the electron accumulation for n-type (p-type) InN surfaces. Sulfur treatment has also been shown to be stable, with no increase in band bending following a month of atmospheric exposure.

In this thesis XPS and Hall effect measurements have been performed to

examine two methods of sulfur treatment on two different InN surfaces. Initial experimental results from treating In-polar c-plane samples in S_2Cl_2 solution presented in chapter 4 showed promise, with reductions in electron accumulation of up to ~53 % observed. However, due to the ex-situ nature of this technique, investigations into the development of sulfur bonds and removal of the oxide layer were inhibited by the many parameters involved in ex-situ immersion of a sample into a solution. The results of this experiment highlighted the need for an investigation with greater control and reproducibility into the interactions of sulfur with InN surfaces in the absence of large amounts of atmospheric contamination. To this end, investigations detailed in chapter 5 using XPS were made into the effects of in-situ deposition of sulfur on InN surfaces using an electrochemical cell. A reduction in band bending of 0.27 eV and 0.23 eV were observed following sulfur deposition on the a-plane and In-polar c-plane surfaces respectively, supported by analysis of the In $3d_{5/2}$ peak FWHMs showing a reduction in plasmon losses associated with the electron accumulation layer. Using the space charge calculations outlined in section 3.2, it was found that this completely removed the electron accumulation layer for the a-plane sample and produced a 55 % reduction at the c-plane surface, which had a larger initial band bending.

The in-situ deposition of sulfur has the advantage over other sulfur treatment techniques that the sample can be studied at intervals throughout the process, giving a detailed insight into the interaction of sulfur atoms at the surface. Indeed, sulfur bonds to indium in the form of In–S–In and In–S–S–In environments were observed, though the preferential bonding configurations differed between the a-plane and In-polar c-plane samples. For the a-plane sample, it was observed that initially an In–S–S–In environment was preferred, however, after 270 L of sulfur exposure this was replaced by In–S–In bonding. On the c-plane sample, the inverse was observed, with the change occurring much earlier, after only ~20 L of sulfur exposure. For the c-plane sample, the relationship between the position of the surface Fermi level and the sulfur exposure was most accurately modelled using a double exponential, with the constants showing that two processes were at work to reduce the surface Fermi level. This was ascribed to the In–S–In and In–S–S–In bonding environments and showed that although the In–S–S–In bonds required more exposure to

form, they acted to reduce the surface Fermi level further than for In–S–In bonding. The exponential fit also indicated the presence of a limit to how far the surface Fermi level could be lowered by depositing sulfur, however it may be possible to reduce that limit through surface preparation techniques.

The structure of the In adlayers has been studied for the In-polar *c*-plane surface, however it not yet been resolved for *a*-plane surface. In this study it was observed that the binding energy of the XPS peaks corresponding to In–S–In bonding in for the *a*-plane sample were at higher binding energy than for the *c*-plane sample, indicating a lesser proximity of valence electrons to screen the core hole left by each emitted photoelectron. This could imply a larger interlayer spacing for the adlayers on the *a*-plane sample, though further structural studies are required in order to draw firm conclusions.

6.1 Future Directions

As mentioned previously, in order to fully understand the favourable sulfur bonding environments and their effect on the surface Fermi level would require techniques such as DFT, STM and ion scattering techniques. However, the large reduction in band bending observed using the in-situ sulfur deposition for both the *a*-plane and In-polar *c*-plane samples shows that this method is promising for device surface preparation. In addition, it is already known that the sulfur content of $(NH_4)_2S_x$ solution varies between manufacturers and can have a great effect on experimental results [98]. Through a greater understanding of the interaction of sulfur at the surface it may be possible to engineer solutions with optimal sulfur content to further reduce the surface Fermi level.

Bibliography

[1] H. Kroemer, Reviews of Modern Physics **73**, 783 (2001).

[2] Z. Alferov, Reviews of Modern Physics **73**, 767 (2001).

[3] V. W. L. Chin, T. L. Tansley, and T. Osotchan, Journal of Applied Physics **75**, 7365 (1994).

[4] V. M. Polyakov and F. Schwierz, Applied Physics Letters **88**, 032101 (2006).

[5] V. M. Polyakov and F. Schwierz, Journal of Applied Physics **99**, 113705 (2006).

[6] R. Ascazubi, I. Wilke, K. Denniston, H. Lu, W. J. Schaff, R. Ascazubi, and R. Ascázubi, Applied Physics Letters **84**, 4810 (2004).

[7] H. Ahn, Y.-P. Ku, Y.-C. Wang, C.-H. Chuang, S. Gwo, and C.-L. Pan, Applied Physics Letters **91**, 132108 (2007).

[8] H. Ahn, Y.-J. Yeh, Y.-L. Hong, and S. Gwo, Applied Physics Letters **95**, 232104 (2009).

[9] G. Xu, Y. J. Ding, H. Zhao, G. Liu, M. Jamil, N. Tansu, I. B. Zotova, C. E. Stutz, D. E. Diggs, N. Fernelius, F. K. Hopkins, C. S. Gallinat, G. Koblmüller, and J. S. Speck, Semiconductor Science and Technology **25**, 015004 (2010).

[10] V. Davydov, A. Klochikhin, V. Emtsev, S. Ivanov, V. Vekshin, F. Bechstedt, J. Furthmüller, H. Harima, A. Mudryi, A. Hashimoto, A. Yamamoto, J. Aderhold, J. Graul, and E. E. Haller, physica status solidi (b) **6**, 6 (2002).

[11] J. Wu, W. Walukiewicz, K. M. Yu, J. W. Ager, E. E. Haller, H. Lu, W. J. Schaff, Y. Saito, and Y. Nanishi, Applied Physics Letters **80**, 3967 (2002).

[12] W. Walukiewicz, J. W. Ager, K. M. Yu, Z. Liliental-Weber, J. Wu, S. X. Li, R. E. Jones, and J. D. Denlinger, Journal of Physics D: Applied Physics **39**, R83 (2006).

[13] J. Wu, W. Walukiewicz, K. M. Yu, W. Shan, J. W. Ager, E. E. Haller, H. Lu, W. J. Schaff, W. K. Metzger, and S. Kurtz, Journal of Applied Physics **94**, 6477 (2003).

[14] X. Chen, K. D. Matthews, D. Hao, W. J. Schaff, and L. F. Eastman, physica status solidi (a) **205**, 1103 (2008).

[15] L. Hsu and W. Walukiewicz, Journal of Applied Physics **104**, 024507 (2008).

[16] J.-K. Sheu, C.-C. Yang, S.-J. Tu, K.-H. Chang, M.-L. Lee, W.-C. Lai, and L.-C. Peng, IEEE Electron Device Letters **30**, 225 (2009).

[17] E. Matioli, C. Neufeld, M. Iza, S. C. Cruz, A. a. Al-Heji, X. Chen, R. M. Farrell, S. Keller, S. DenBaars, U. Mishra, S. Nakamura, J. Speck, and C. Weisbuch, Applied Physics Letters **98**, 021102 (2011).

[18] T. Miyoshi, S. Masui, T. Okada, T. Yanamoto, T. Kozaki, S.-i. Nagahama, and T. Mukai, Applied Physics Express **2**, 062201 (2009).

[19] A. Khan, Nature Photonics **3**, 432 (2009).

[20] R. Jones, K. Yu, S. Li, W. Walukiewicz, J. Ager, E. Haller, H. Lu, and W. Schaff, Physical Review Letters **96**, 125505 (2006).

[21] P. D. C. King, T. D. Veal, H. Lu, P. H. Jefferson, S. A. Hatfield, W. J. Schaff, and C. F. McConville, physica status solidi (b) **245**, 881 (2008).

[22] P. D. C. King, T. D. Veal, P. H. Jefferson, C. F. McConville, H. Lu, and W. J. Schaff, Physical Review B **75**, 115312 (2007).

[23] W. M. Linhart, J. Chai, R. J. H. Morris, M. G. Dowsett, C. F. McConville, S. M. Durbin, and T. D. Veal, Physical Review Letters **109**, 247605 (2012).

[24] K. Momma and F. Izumi, Journal of Applied Crystallography **44**, 1272 (2011).

[25] C. G. Van de Walle and D. Segev, Journal of Applied Physics **101**, 081704 (2007).

[26] H. J. Hove and J. J. Cuomo, Applied Physics Letters **20**, 71 (1972).

[27] V. A. Tyagi, A. M. Eustigneev, A. N. Krasilo, A. F. Andreeva, and V. Y. Malatidiou, Soviet Physics - Semiconductors **11**, 1257 (1977).

[28] K. L. Westra, R. P. W. Lawson, and M. J. Brett, Journal of Vacuum Science & Technology A **6**, 1730 (1988).

[29] H. Morkoç, *Nitride Semiconductors and Devices*, Springer Series in Materials Science, Vol. 32 (Springer, Berlin, Heidelberg, 1999).

[30] T. L. Tansley and C. P. Foley, Journal of Applied Physics **59**, 3241 (1986).

[31] T. D. Veal, C. F. McConville, and W. J. Schaff, *Indium Nitride and Related Alloys* (CRC Press/Taylor & Francis, Boca Raton, 2010).

[32] S. Yamaguchi, M. Kariya, S. Nitta, T. Takeuchi, C. Wetzel, H. Amano, and I. Akasaki, Applied Physics Letters **76**, 876 (2000).

[33] T. Matsuoka, H. Tanaka, T. Sasaki, and A. Katsui, in *Inst. Phys. Conf. Ser* (1990) pp. Vol. 106, p. 141.

[34] H. Lu, W. J. Schaff, J. Hwang, H. Wu, G. Koley, and L. F. Eastman, Applied Physics Letters **79**, 1489 (2001).

[35] V. Y. Davydov, A. A. Klochikhin, R. P. Seisyan, and V. V. Emtsev, physica status solidi (b) **3**, 1972 (2002).

[36] Y. Nanishi, Y. Saito, and T. Yamaguchi, Japanese Journal of Applied Physics **42**, 2549 (2003).

[37] J. Wu, W. Walukiewicz, W. Shan, K. M. Yu, J. W. Ager, S. X. Li, E. E. Haller, H. Lu, and W. J. Schaff, Journal of Applied Physics **94**, 4457 (2003).

[38] E. Burstein, Physical Review **93**, 632 (1954).

[39] T. S. Moss, Proceedings of the Physical Society. Section B **67**, 775 (1954).

[40] W. Walukiewicz, Applied Physics Letters **54**, 2094 (1989).

[41] M. Born and R. Oppenheimer, Annalen der Physik **389**, 457 (1927).

[42] P. Y. Yu and M. Cardona, *Fundamentals of Semiconductors: Physics and Materials Properties* (Springer, 1999).

[43] V. Heine, Physical Review **138**, A1689 (1965).

[44] F. Flores and C. Tejedor, Journal of Physics C: Solid State Physics **12**, 731 (1979).

[45] J. Tersoff, Physical Review Letters **52**, 465 (1984).

[46] C. G. Van de Walle and J. Neugebauer, Nature **423**, 626 (2003).

[47] P. D. C. King, T. D. Veal, P. H. Jefferson, S. A. Hatfield, L. F. J. Piper, C. F. McConville, F. Fuchs, J. Furthmüller, F. Bechstedt, H. Lu, and W. J. Schaff, Physical Review B **77**, 045316 (2008).

[48] H. Lüth, *Surfaces and Interfaces of Solid Materials*, Springer study edition (Springer, Berlin, Heidelberg, New York, 1997).

[49] I. Mahboob, T. D. Veal, C. F. McConville, H. Lu, and W. J. Schaff, Physical Review Letters **92**, 036804 (2004).

[50] I. Mahboob, T. D. Veal, L. F. J. Piper, C. F. McConville, H. Lu, W. J. Schaff, J. Furthmuller, and F. Bechstedt, Physical Review B **69**, 201307 (2004).

[51] L. Colakerol, T. D. Veal, H.-K. Jeong, L. Plucinski, A. DeMasi, T. Learmonth, P.-A. Glans, S. Wang, Y. Zhang, L. F. J. Piper, P. H. Jefferson,

A. Fedorov, T.-C. Chen, T. D. Moustakas, C. F. McConville, and K. E. Smith, Physical Review Letters **97**, 237601 (2006).

[52] T. D. Veal, P. D. C. King, M. Walker, C. F. McConville, H. Lu, and W. J. Schaff, Physica B-Condensed Matter **401**, 351 (2007).

[53] D. Segev and C. G. Van De Walle, Europhysics Letters (EPL) **76**, 305 (2006).

[54] C.-L. Wu, H.-M. Lee, C.-T. Kuo, C.-H. Chen, and S. Gwo, Physical Review Letters **101**, 106803 (2008).

[55] A. Eisenhardt, M. Himmerlich, and S. Krischok, physica status solidi (a) **209**, 45 (2012).

[56] W. Walukiewicz, Journal of Vacuum Science & Technology B: Microelectronics and Nanometer Structures **5**, 1062 (1987).

[57] T. D. Veal, P. D. C. King, P. H. Jefferson, L. F. J. Piper, C. F. McConville, H. Lu, W. J. Schaff, P. A. Anderson, S. M. Durbin, D. Muto, H. Naoi, and Y. Nanishi, Physical Review B **76**, 075313 (2007).

[58] V. Lebedev, C. Y. Wang, V. Cimalla, S. Hauguth, T. Kups, M. Ali, G. Ecke, M. Himmerlich, S. Krischok, J. A. Schaefer, O. Ambacher, V. M. Polyakov, and F. Schwierz, Journal of Applied Physics **101**, 123705 (2007).

[59] V. Cimalla, V. Lebedev, C. Y. Wang, M. Ali, G. Ecke, V. M. Polyakov, F. Schwierz, O. Ambacher, H. Lu, and W. J. Schaff, Applied Physics Letters **90**, 152106 (2007).

[60] A. Denisenko, C. Pietzka, A. Chuvilin, U. Kaiser, H. Lu, W. J. Schaff, and E. Kohn, Journal of Applied Physics **105**, 033702 (2009).

[61] A. Eisenhardt, S. Reiß, M. Himmerlich, J. A. Schaefer, and S. Krischok, physica status solidi (a) **207**, 1037 (2010).

[62] L. Pauling, Journal of the American Chemical Society **481**, 3570 (1932).

[63] H. Oigawa, J. Fan, Y. Nannichi, H. Sugahara, and M. Oshima, Japanese Journal of Applied Physics **30**, 322 (1991).

[64] M. J. Lowe, T. D. Veal, C. F. McConville, G. R. Bell, S. Tsukamoto, and N. Koguchi, Surface Science **523**, 179 (2003).

[65] D. Petrovykh, J. M. Sullivan, and L. J. Whitman, Surface and Interface Analysis **37**, 989 (2005).

[66] L. R. Bailey, T. D. Veal, C. E. Kendrick, S. M. Durbin, and C. F. McConville, Applied Physics Letters **95**, 192111 (2009).

[67] Y.-H. Chang, Y.-S. Lu, Y.-L. Hong, C.-T. Kuo, S. Gwo, and J. A. Yeh, Journal of Applied Physics **107**, 043710 (2010).

[68] W. M. Linhart, J. Chai, C. F. McConville, S. M. Durbin, and T. D. Veal, Journal of Applied Physics **114**, 103702 (2013).

[69] L. R. Bailey, T. D. Veal, and C. F. McConville, physica status solidi (c) **8**, 1605 (2011).

[70] M. P. Seah and W. A. Dench, Surface and Interface Analysis **1**, 2 (1979).

[71] N. Fairley, http://www.casaxps.com (2010).

[72] D. P. Woodruff and T. A. Delchar, *Modern Techniques of Surface Science*, Cambridge Solid State Science Series (Cambridge University Press, 1994).

[73] P. D. C. King, T. D. Veal, H. Lu, S. A. Hatfield, W. J. Schaff, and C. F. McConville, Surface Science **602**, 871 (2008).

[74] S. A. Chambers, T. Droubay, T. C. Kaspar, and M. Gutowski, Journal of Vacuum Science & Technology B **22**, 2205 (2004).

[75] D. A. Shirley, Physical Review B **5**, 4709 (1972).

[76] J. C. Vickerman, *Surface Analysis: The Principal Techniques*, edited by J. C. Vickerman and I. S. Gilmore (John Wiley & Sons, Ltd, Chichester, UK, 2009).

[77] K. Siegbahn, C. Nordling, A. Fahlman, R. Nordberg, K. Hamrim, J. Hedman, C. Johansson, T. Bergmark, S. E. Karlsson, I. Lindgren, and B. Lindberg, *ESCA: Atomic, Molecular and Solid State Structure Studied by Means of Electron Spectroscopy* (Almqvist & Wiksells, Uppsala, 1967).

[78] M. Seah and M. Anthony, Surface and Interface Analysis **6**, 24 (1984).

[79] J. H. Scofield, Journal of Electron Spectroscopy and Related Phenomena **8**, 129 (1976).

[80] E. Hall, American Journal of Mathematics **2**, 287 (1879).

[81] N. W. Ashcroft and N. D. Mermin, *Solid State Physics* (Saunders College, 1976).

[82] L. J. van der Pauw, Philips Technical Review **20**, 220 (1958).

[83] G. Paasch and H. Übensee, physica status solidi (b) **113**, 165 (1982).

[84] E. Kane, Journal of Physics and Chemistry of Solids **1**, 249 (1957).

[85] P. D. C. King, T. D. Veal, and C. F. McConville, Physical Review B **77**, 125305 (2008).

[86] G. R. Bell, C. F. McConville, and T. S. Jones, Physical Review B **54**, 2654 (1996).

[87] G. R. Bell, C. F. McConville, C. P. A. Mulcahy, and T. S. Jones, Journal of Physics: Condensed Matter **9**, 2903 (1997).

[88] M. M. Hyland and G. Bancroft, Geochimica et Cosmochimica Acta **53**, 367 (1989).

[89] J. Sharma, D. S. Downs, Z. Iqbal, and F. J. Owens, The Journal of Chemical Physics **67**, 3045 (1977).

[90] V. Nefedov, D. Gati, B. Dzhurinskii, N. Sergushin, and Y. Salyn, Zh. Neorg. Khim. **20**, 2307 (1975).

[91] C. D. Wagner, D. A. Zatko, and R. H. Raymond, Analytical Chemistry **52**, 1445 (1980).

[92] M. Katayama, M. Aono, H. Oigawa, Y. Nannichi, H. Sugahara, and M. Oshima, Japanese Journal of Applied Physics **30**, L786 (1991).

[93] M. Shimomura, K. Naka, N. Sanada, Y. Suzuki, Y. Fukuda, and P. J. Moller, Journal of Applied Physics **79**, 4193 (1996).

[94] W. Schaff, H. Lu, L. F. Eastman, W. Walukiewicz, K. M. Yu, S. Keller, S. Kurtz, B. Keyes, and L. Gevilas, in *State-of-the-Art Program on Compound Semiconductors XLI and Nitride and Wide Bandgap Semiconductors for Sensors, Photonics and Electronics V: Proceedings of the International Symposia, Volume 2004* (The Electrochemical Society, 2004) p. 358.

[95] C. Wagner, The Journal of Chemical Physics **21**, 1819 (1953).

[96] D. Detry and J. Drowart, Zeitschrift für Physikalische Chemie **55**, 314 (1967).

[97] A. Eisenhardt, S. Krischok, and M. Himmerlich, Applied Physics Letters **102**, 231602 (2013).

[98] R. Iyer and D. L. Lile, Applied Physics Letters **59**, 437 (1991).